Engineering xxx (xxxx) xxx

Contents lists available at ScienceDirect

Engineering

journal homepage: www.elsevier.com/locate/eng

Article

Mechanism Design and Motion Planning of a Hexapod Curling Robot Exhibited during the Beijing 2022 Winter Olympics

Ke Yin [a], Yue Gao [a,*], Feng Gao [b,*], Xianbao Chen [b], Yue Zhao [a], Yuguang Xiao [b], Qiao Sun [b], Jing Sun [b]

[a] School of Electronic Information and Electrical Engineering, Shanghai Jiao Tong University, Shanghai 200240, China
[b] Key Laboratory of Mechanical System and Vibration, School of Mechanical Engineering, Shanghai Jiao Tong University, Shanghai 200240, China

ARTICLE INFO

Article history:
Received 6 February 2023
Revised 26 August 2023
Accepted 17 October 2023
Available online xxxx

Keywords:
Legged robot
Curling robot
Winter Olympics
Mechanism design
Motion planning

ABSTRACT

When a curling rock slides on an ice sheet with an initial rotation, a lateral movement occurs, which is known as the curling phenomenon. The force of friction between the curling rock and the ice sheet changes continually with changes in the environment; thus, the sport of curling requires great skill and experience. The throwing of the curling rock is a great challenge in robot design and control, and existing curling robots usually adopt a combination scheme of a wheel chassis and gripper that differs significantly from human throwing movements. A hexapod curling robot that imitates human kicking, sliding, pushing, and curling rock rotating was designed and manufactured by our group, and completed a perfect show during the Beijing 2022 Winter Olympics. Smooth switching between the walking and throwing tasks is realized by the robot's morphology transformation based on leg configuration switching. The robot's controlling parameters, which include the kicking velocity v_k, pushing velocity v_p, orientation angle θ_c, and rotation velocity ω, are determined by aiming and sliding models according to the estimated equivalent friction coefficient μ_{equ} and ratio e of the front and back frictions. The stable errors between the target and actual stopping points converge to 0.2 m and 1.105 m in the simulations and experiments, respectively, and the error shown in the experiments is close to that of a well-trained wheelchair curling athlete. This robot holds promise for helping ice-makers rectify ice sheet friction or assisting in athlete training.

1. Introduction

Curling is a very challenging Winter Olympics sport, commonly known as "chess on ice". When a curling rock is thrown with a clockwise rotation on an ice sheet, a lateral movement to the right will occur; this is known as the "curling phenomenon". The curling phenomenon is anomalous, as the trajectory will deflect to the left when the rock slides on a table. What is even more difficult for researchers to explain is that the deflection distance of the curling rock on a table is positively correlated with the rotation speed, whereas the curling distance (a typical value of 0.9–1.2 m) on an ice sheet is weakly dependent upon the rotation speed. Currently, there are two kinds of methods used to explain the curling trajectory: the intuitive model and the first-principles model.

The intuitive model uses a hypothesis model to predict the curling trajectory but does not consider the microscopic mechanism of the friction between the running band at the bottom of the curling rock and the ice sheet. The running band is a ring-shaped annulus (with a radius of 60 mm and a width of 6 mm) at the bottom of the curling rock, which is scratched to obtain a proper roughness in order to reach the standard curling distance. The intuitive model generally considers that the friction force between the curling rock and the ice sheet is unevenly distributed along the circumference of the running band. Denny [1,2] reported two different models to explain the curling phenomenon, but the friction coefficients in the two models were different. The researchers first proposed a right-left friction model, but it failed to generate a net sideward force. They subsequently introduced a front-rear friction asymmetry model when considering the impact of ice debris, which was able to explain the curling direction when the rear friction was greater than the front friction. Maeno [3,4] proposed that the front-rear friction was asymmetrical, but they argued that the greater friction on the rear half resulted from a temperature reduction when the liquid film formed by the leading half evaporated. More specifically, a reduced temperature of 1°C would lead to a 26% increase in friction on the rear half at a low sliding speed of 1 m·s^{-1}. Penner [5] proposed a sliding cylinder model, which successfully explained the lateral deflection of a rotating upside-down glass when sliding over a dry horizontal table, but had difficulty

* Corresponding authors.
E-mail addresses: yuegao@sjtu.edu.cn (Y. Gao), fengg@sjtu.edu.cn (F. Gao).

https://doi.org/10.1016/j.eng.2023.10.018
2095-8099/

Please cite this article as: K. Yin, Y. Gao, F. Gao et al., Mechanism Design and Motion Planning of a Hexapod Curling Robot Exhibited during the Beijing 2022 Winter Olympics, Engineering, https://doi.org/10.1016/j.eng.2023.10.018

explaining the curling phenomenon. Shegelski et al. [6] proposed that the friction changes resulted from the formation of a liquid film between the running band and the ice sheet. They considered a pure friction magnitude asymmetry model that varied along with the circumference of the running band at first, and then modified the model by adding variation in the friction direction [7,8]. Nevertheless, these explanations based on a liquid film are controversial, since the existence of a quantity of liquid water that could satisfy the proposed mechanism has not been confirmed experimentally. Furthermore, these models have a general problem: They are strongly dependent on the angular velocity of the curling rock. To weaken this dependence, a pivot-slide model based on two physical processes—a brief pivot of the rock around a point beneath the running band followed by a longer sliding—was recently put forward by Shegelski and Lozowski [9]. However, a fixed curling distance of 1 m was introduced into the equations, resulting in no dependence on the initial angular velocity. Mancini and Schoulepnikoff [10] improved the pivot-slide model and considered that the ratio of the pivot to the sliding time was dependent on the rock speed, but there was a systematic discrepancy in the longitudinal distance and rotation speed between the experiment and the model.

The first-principles model focuses on the interaction between the pebbles beneath the running bond and the ice sheet. A scratch-guiding model was proposed by Nyberg et al. [11], who considered that the scratches caused by the roughness on the leading half of the band would exert an interaction force with the roughness on the trailing half, which could result in a deviation in the curling direction. Cross-scratches were clearly observed by directly scanning the ice surface with a white light interferometer [12]. However, the calculation of friction is relatively difficult and complex for irregular pebble shapes and requires further study. To sum up, because the friction of a curling rock is contrary to ordinary tribology, no accepted model has been developed to fully explain the curling phenomenon.

With the continuous expansion of robot application, emerging robots have been developed for different fields. Sport robots, which can provide companionship and entertainment for athletes, are considered to be one of the most promising areas of robotics. Thus far, robots have been successfully used to play football and baseball, and even do alpine skiing. In the sport of curling, it is difficult for players to precisely control the complicated curling trajectory, as suggested by the above analysis; however, this is much easier for a robot due to its high control accuracy and repeatability. Kawamura et al. [13] designed a fixed mechanism to throw a curling rock. Its main units are roughly classified as a delivering board, a linear guide, a frame, a delivery direction change mechanism, a pushing-out mechanism, and a rotation-applying mechanism. The mechanism is fixed to the mounting hole of the hack (i.e., the kicking board for a throw) on the curling sheet. In a human-robot match, the athlete and the robot share a hack, and frequent disassembly of the entire device greatly reduces the fun and efficiency. Compared with a fixed machine, robots using a mobile platform are more flexible and convenient when conducting alternate human-robot throws.

Mobile robots can be divided into four categories according to their driving methods: tracked, wheeled, legged, and wheel-legged. Tracked robots are clearly not suitable for curling throwing, as their tracks can easily damage the ice surface. One- or two-wheeled robots [14–16], which have mechanical instability and control complexity due to their use of the inverse pendulum concept, are also unsuitable for curling throwing, which requires stability and high-precision motion control. In comparison, three- or four-wheeled robots are acceptable for curling throwing. Harbin Institute of Technology developed a four-wheeled curling robot, which combined a wheeled universal chassis and a gripper. This chassis uses deep-tread tires to increase friction, but this reduces the control accuracy. Choi et al. [17,18] designed a three-wheeled curling robot composed of a gripper, chassis, and camera arm. A slip ratio controller was adopted to prevent slippage based on the difference between the wheel and robot speeds. These two robots were able to control the throwing velocity and the heading direction of the curling rock, but the curling direction was random and uncontrollable due to the lack of initial rotation of the curling rock. The gripper of the three-wheeled robot was further improved by Won et al. [19,20] to obtain the rotation ability; its throwing velocity, direction and rotation velocity were given by a carried artificial intelligence (AI) system. In general, the wheeled robot has advantages in stability, but a slipping phenomenon was observed. Moreover, this robot can damage the delicate surface of the ice, since the robot's forward energy comes from the friction between the wheel and the ice surface.

Legged mobile robots may hold promise for application in curling throwing due to their flexible configuration transformation. Such robots usually are divided into biped robots [21,22], quadruped robots [23,24], hexapod robots [25,26], and octopod robots [27]. Considering that at least two legs are needed to imitate the gripper and three legs to support the body in curling throwing, a hexapod or octopod robot is clearly more reasonable for the task. Two [28], four [29,30], or six wheel-legged robots [31,32] have exhibited excellent performance in terrain adaptability and rapidity. Thanks to their intrinsic characteristics of system stability and leg reusability, along with the theories supporting their design, control, gait planning, and obstacle avoidance methods, as proposed by researchers such as Chen et al. [31,32], six-wheel-legged robots are likely to be applied to the sport of curling. When comparing octopod robots and six-wheel-legged robots, our team finally chose to use a hexapod robot to throw the curling rock because of this robot's relatively simply mechanism and control.

In this research, a hexapod curling robot was designed to imitate human throwing movements, including kicking the hack with the leg and pushing and rotating the curling rock with the arm [33]. This robot obtains forward energy from the reaction force between the rear legs and the hack, instead of the friction between the tiptoe and the ice surface, thereby avoiding damage to the ice sheet. To complete the throwing, the hexapod robot must move to the hacks using a 3-3 gait on the ice surface, and then crawl on the ice with its two front legs grasping and throwing the rock. Hence, a morphology transformation between a hexapod and quadruped robot is necessary for the alternant cyclic walking and throwing. The robot's functions of gripping and releasing the curling rock and supporting, accelerating, and slowing down the robot body are achieved by means of a multi-functional leg design [34]. One throwing task involves aiming in the target direction, the collaborative sliding of the robot and rock, and the individual sliding of the rock, so corresponding analytical equation models are established. The input parameters in the robot control system, including the aiming angle, the kicking velocity with the rear legs, and the pushing velocity with the front legs, are calculated from the estimated equivalent friction coefficient and the ratio of rear and front friction. The friction state is reappraised by means of a PI controller based on the historical throwing results. The stable errors individually converge to 0.2 m and 1.105 m in throwing simulations and experiments by means of feedback control. Our curling robot has a wide range of application scenarios. It can be used as an entertainment robot to compete with humans, creating novel and interesting experiences for players. Human-robot matches are also helpful for athletes to improve their training strategies. Another extremely important application is to replace athletes in assisting ice makers in ice making, as the process of laying the ice surface requires excellent athletes to throw a curling rock at fixed points to detect the curling state of the ice surface.

2. Robot design

As shown in Fig. 1, the hexapod curling robot has a weight of 75 kg, a body length of 0.6 m, and a body width of 0.3 m. The shank and thigh of the front and middle legs are the same lengths (0.3 m), while those of the rear legs are 0.5 m to obtain a longer sprint distance. The robot has 21 motors in total, of which 18 are mounted on the hips to generate the leg motions, two are mounted on the knees of the front legs to rotate the curling rock, and the remaining one is mounted on the body to actuate the arm. Three integrated drive units (IDUs), mainly composed of a direct current DC motor, a harmonic reducer, an absolute encoder, a driver, and torque sensors, are utilized to provide precise torque output for each leg. The three motors on the knee and body work at the velocity mode for simpler and cheaper control. The inertial measurement unit (IMU) is mounted on the body to obtain the actual body posture. The right rear leg is numbered 1, and the other legs are numbered from 2 to 6 in counterclockwise order.

2.1. Rock-throwing movement

Human curling athletes use a skillful method to throw curling rocks. As shown in Fig. 2(a), two special shoes made of different materials are worn on the feet. A rubber shoe is worn on the rear leg to provide relatively high friction in order to speed up the body, while a plastic shoe is worn on the front leg with a small friction to support the sliding of the body. The detailed method is illustrated in Fig. 2(b): First, the player aims at the target point that is marked with an ice broom by the other teammate. Then, the player kicks the hack with his/her rear leg, while grabbing the handle of the curling rock with one hand and an ice broom with the other hand to balance the body. Next, the player slides forward with the curling rock under the only constraint of friction. Lastly, the player pushes the curling rock to speed it up again and rotates it in a certain curling direction before reaching the hog line.

Inspired by the human movements, the robot uses a similar method to throw a curling rock. First, the robot aims in the target direction by means of a vision system consisting of a laser radar and a camera. The radar is used to recognize the current positions of the curling rocks on the ice sheet, while the camera is used to distinguish the curling rocks by color. An arm installed on the backside of the robot's body is extended upward before aiming to broaden the camera's view for observing all the curling rocks (Fig. 3(a)); it is then retracted downward after aiming (Fig. 3(b)). Next, the two driving wheels on the front legs begin to actuate the curling rock rotation. Then, the rear legs exhaust to kick the hack, and the combined system—including the robot and the curling rock—sprints forward under the reaction force from the hack (Fig. 3(c)). Subsequently, the velocity of the combined system gradually decreases under the action of friction. Lastly, the front legs push the curling rock and speed it up again before reaching the hog line (Fig. 3(d)).

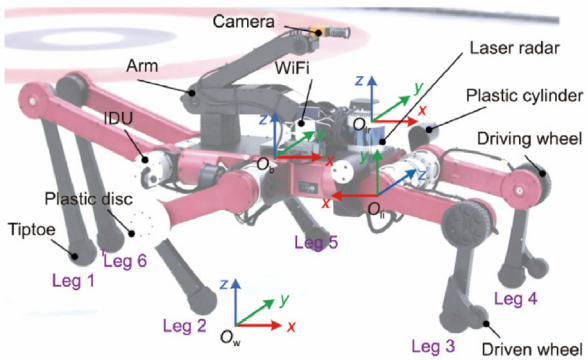

Fig. 1. The hexapod curling robot.

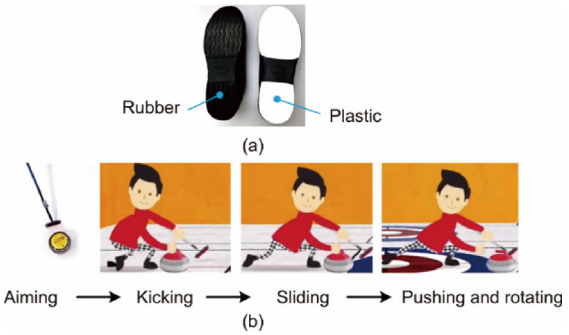

Fig. 2. Human movement when throwing a curling rock.

2.2. Morphology transformation

The hexapod curling robot was designed with two main functions: walking and throwing. The robot walks to the curling sheet from outside the stadium or returns to the hack region after one throw through using a 3-3 gait [35,36], as is widely done in other hexapod robots. The robot morphology is denoted in Fig. 4(a); the body is alternatively supported by the triangles 1-3-5 or 2-4-6 (formed by corresponding footholds). Figs. 4(b) and (c) shows the transitional morphologies from walking to throwing. First, the middle legs at 2 and 5 switch to the 'L' configuration from the 'anti-L' configuration (introduced in Section 2.3) to rearrange the center of mass (CoM) position from morphology 1-3-4-6 to morphology 1-2-5-6, while the front and rear legs support the body in a rectangular morphology. Then, the two front legs fold to the preparation posture for grabbing the curling rock, while the middle and rear legs support the body. Next, the robot decreases its body height until the plastic cylinders in the front legs touch the ground; the middle legs then switch to 'anti-L' configuration again when the cylinders of the front legs and the tiptoes of the rear legs are supporting the body (Fig. 4(d)). Lastly, the robot enters the preparation morphology for throwing the curling rock, in which the plastic cylinders of the front legs and the plastic discs of the middle legs provide four slippery supporting points, and the two rear legs with a rubber tiptoe kick the hack and hold the position above the ice during sliding.

2.3. Leg mechanism design

A four-bar linkage is widely used as the leg mechanism in the sagittal plane for agile legged robots such as Zhao et al. [37], Mao et al. [38], Arm et al. [39], Kolvenbach et al. [40], and Boaventura et al. [41]. It works well in these running robots because it is not necessary to switch the leg configuration while running at high speed. In the hexapod curling robot, it is vital for the leg configuration to switch between the 'L' and 'anti-L' configurations for morphology switching (Section 2.2), in order to rearrange the CoM position to avoid robot instability. However, the four-bar linkage cannot actively switch configurations, since the pressure angle is equal to 90° at the switch moment; hence, a special leg mechanism was designed to solve the configuration switch problem. As shown in Fig. 5(a), θ_a, θ_t and θ_s are the abduction, thigh and shank angles, respectively. The leg coordinate frame system in body and sagittal plane of leg are denoted by O_{xyz} and O_{s-xyz}. The location A is the connection position between body and leg. The location B is the hip position. The C_1 (C_2) is the intersection point between rocker

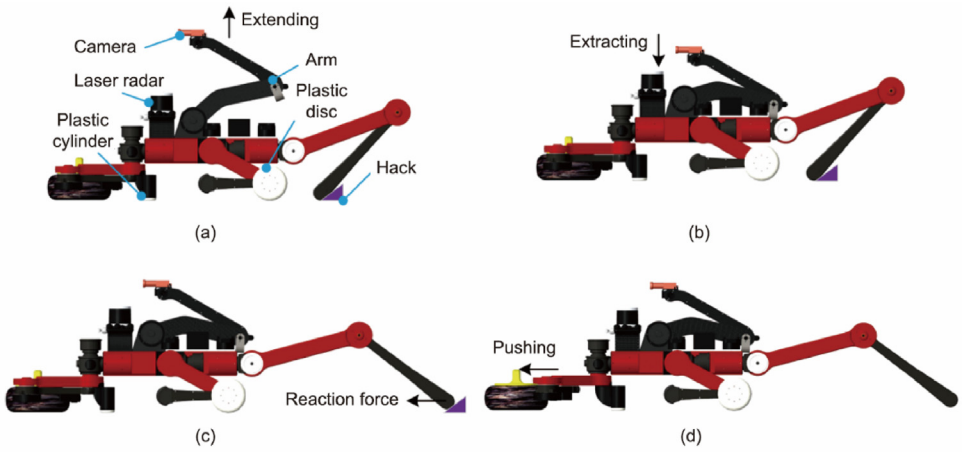

Fig. 3. The robot's movements when throwing a curling rock.

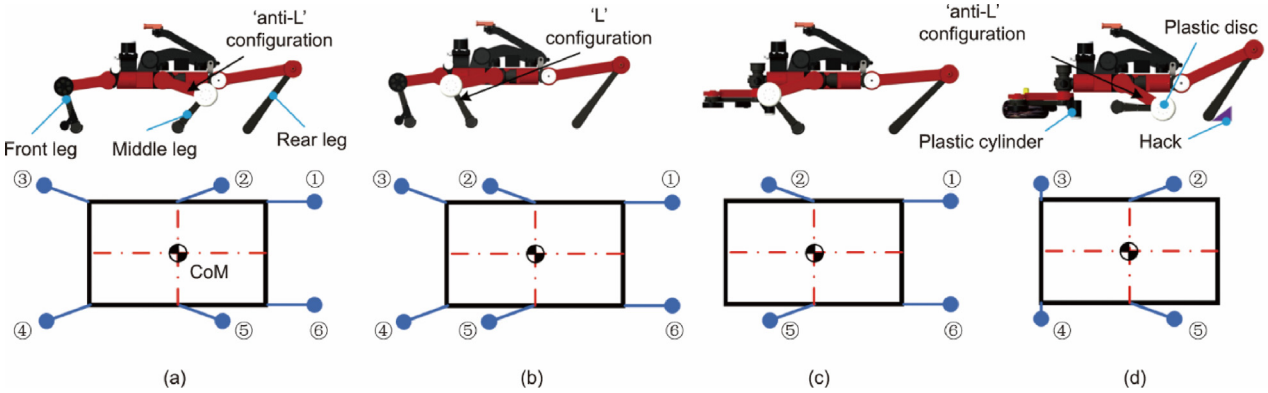

Fig. 4. The morphology transformation of the robot legs between different tasks.

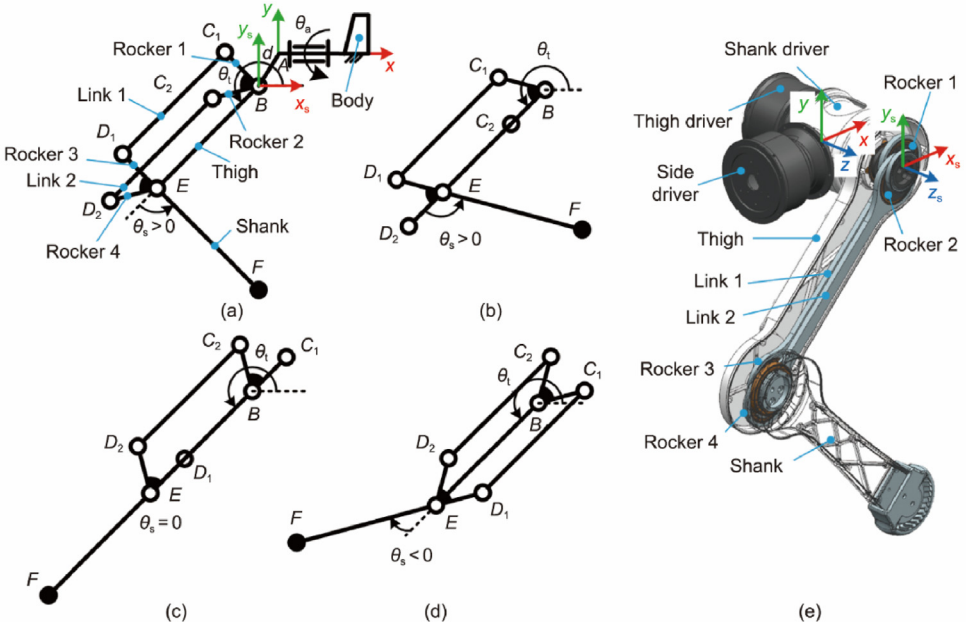

Fig. 5. The configuration switching principle of the leg mechanism.

1 (rocker 2) and link 1 (link 2) while the D_1 (D_2) is the intersection point between rocker 3 (rocker 4) and link 1 (link 2). The location E is the intersection point between thigh and shank. The F denotes the tiptoe position. Two parallelogram mechanisms BC_1D_1E and BC_2D_2E were designed to actuate the shank together. More specifically, rocker 1 and rocker 2 are actuated by the shank driver and

maintain a constant angle at all times. A similar design is used in rocker 3 and rocker 4. The advantage of this design is that at least one parallelogram mechanism is always involved in the driving of the shank. When a parallelogram mechanism degenerates into a linear mechanism (i.e., when link D_2E coincides with link C_2D_2 in Fig. 5(b) or when link D_1E coincides with link C_1D_1 in Fig. 5(c)), the pressure angle of the other parallelogram mechanism remains acute, so that the shank can be actuated to pass the coincidence posture. The 'L' and 'anti-L' leg configurations are shown in Figs. 5 (a) and (d), respectively, and the detailed virtual prototype design is illustrated in Fig. 5(e).

2.4. The multi-functional leg design

In addition to the walking function, the six legs of the curling robot are designed with a specific reuse function. As shown in Fig. 6(a), a driving wheel is installed on the knee, while a driven wheel is installed on the tiptoe and a plastic cylinder is installed on the hip. When throwing, the two front legs are folded such that the four driving and driven wheels form a quadrilateral envelope to grab the curling rock (Figs. 6(b) and (c)). Then, the two driving wheels rotate in the same direction to actuate the curling rock, and the two plastic cylinders stand up to support the body. Before reaching the hog line, the curling rock is pushed forward with an extra velocity by the two driven wheels, while the rock is separated from the robot.

As shown in Fig. 7(a), a plastic disc is fixed on the knee of the middle leg. When the robot slides on the ice sheet, the rubber tiptoe is retracted like a landing gear, and the slippery plastic disc touches the ice to support the body (Fig. 7b)). The cooperation between the plastic disc and the cylinder is shown in Fig. 3 After the curling rock has separated from the robot, the rubber tiptoe of the middle leg will touch the ice sheet to quickly slow down the robot body (Fig. 7c)).

When throwing the curling rock, the rear legs kick the hack from the position shown in Fig. 8(a) to that shown in Fig. 8(b). At the end of the kicking motion, a slight gap is planned to get the rubber tiptoe off the ice sheet. Similar to the tiptoe of the middle leg, the tiptoe of the rear leg touch the ground to decrease the sliding velocity of the robot after throwing the curling rock.

3. Modeling

When the robot throws a curling rock, it passes through three stages: the robot aiming, the robot and rock sliding together, and the rock sliding alone. The corresponding three models were established as follows to predict the rock trajectory.

3.1. Modeling the robot aiming

The aiming process is shown in Fig. 9. The rear legs of the robot are close to the hack, and the body of the robot must rotate angle θ_c (the corrective angle for aiming) around the center point O_c between the two rear legs to make the robot body face the targeted direction. The robot position before this rotation is denoted by a green dotted line, while the position after this rotation is denoted by a blue solid line. The O_{b1}/O_{b2} denote the body center before/after the rotation. O_{lr-xyz} and O_{w-xyz} are the laser and world coordinate frame system. It should be noted that, if the robot rotates around the body center O_{b1}, the tiptoes of the rear legs will be far away from the hack. The target position ${}^{lr}\boldsymbol{P}_t = [\ {}^{lr}x_t \quad {}^{lr}y_t \quad {}^{lr}z_t\ ]^T$ is given by a vision system in laser radar coordinate frame O_{lr-xyz}; its position in the world coordinate frame O_{w-xyz} can be written as follows:

$$\boldsymbol{P}_t = {}^{w}\boldsymbol{R}_{b1}\left({}^{lr}\boldsymbol{P}_t + [d_{lr}\ 0\ 0]^T\right) + \boldsymbol{P}_{b1} \tag{1}$$

where d_{lr} is the distance in the x direction between the origin of the body and laser radar coordinate frame, and ${}^{w}\boldsymbol{R}_{b1}$ and $\boldsymbol{P}_{b1}$ are respectively the posture and position of the robot body in the world coordinate frame. The targeted angle θ_c can then be obtained according the method given in Section 4.3.

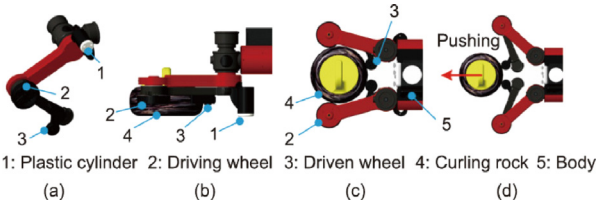

Fig. 6. The multiple functions of the front legs.

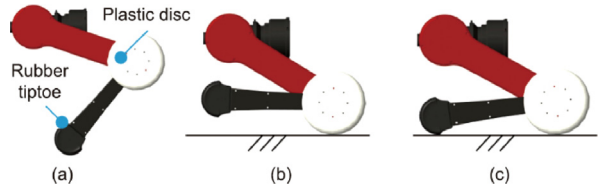

Fig. 7. The multiple functions of the middle legs.

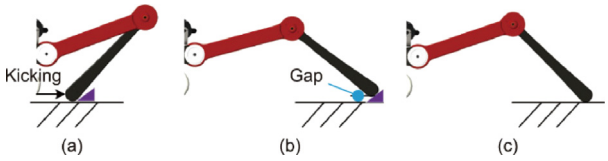

Fig. 8. The multiple functions of the rear legs.

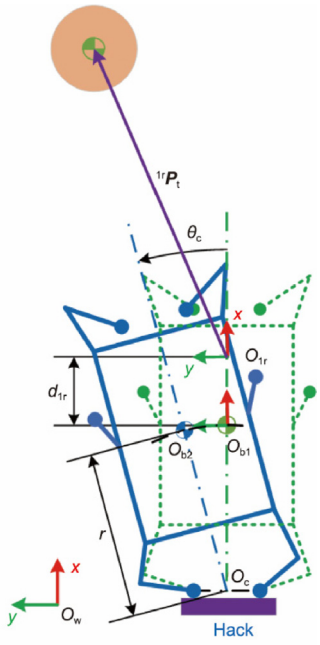

Fig. 9. Planning the robot aiming.

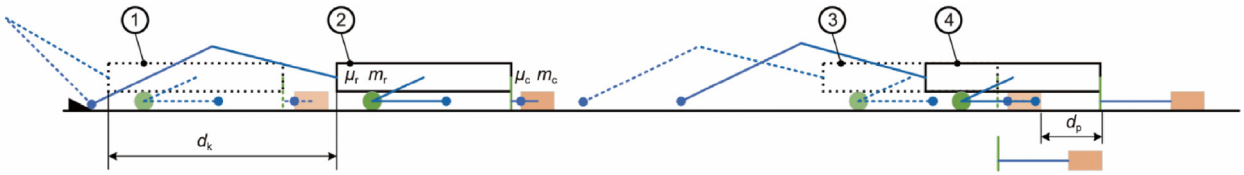

Fig. 10. The movement process of the robot-rock combination system. u_r, u_c, m_r, and m_c are the friction coefficients and masses of the robot and curling rock, respectively.

The tiptoe position of the ith leg in the world coordinate frame before the rotation is denoted as $\boldsymbol{P}_{\text{tipi}}$ $(i = 1, 2, 3, 4, 5 \text{ or } 6)$. The position of O_c $(\boldsymbol{P}_c)$ can be obtained by this equation:

$$\boldsymbol{P}_c = \frac{(\boldsymbol{P}_{\text{tip1}} + \boldsymbol{P}_{\text{tip6}})}{2} \tag{2}$$

The rotation radius (r) can be written as follows:

$$r = \|\boldsymbol{P}_{\text{b1}} - \boldsymbol{P}_c\|_2 \tag{3}$$

The body position change in the body coordinate frame $O_{\text{b1-xyz}}$ after the rotation can be obtained by this equation:

$$\text{b1}\boldsymbol{P}_{\text{b2}} = \begin{bmatrix} r(\cos\theta_c - 1) \\ r\sin\theta_c \\ 0 \end{bmatrix} \tag{4}$$

The new body position $(\boldsymbol{P}_{\text{b2}})$ after the rotation can be written as follows:

$$\boldsymbol{P}_{\text{b2}} = \boldsymbol{P}_{\text{b1}} + {}^{\text{w}}\boldsymbol{R}_{\text{b1}}{}^{\text{b1}}\boldsymbol{P}_{\text{b2}} \tag{5}$$

The new tiptoe position after rotation can be obtained by these equations:

$$\begin{cases} \boldsymbol{P}'_{\text{tipi}} = \boldsymbol{P}_{\text{b2}} + \boldsymbol{P}_{\text{tipi}} - \boldsymbol{P}_{\text{b1}} (i = 2, 3, 4, 5) \\ \boldsymbol{P}'_{\text{tipi}} = \boldsymbol{P}_{\text{tipi}} (i = 1, 6) \end{cases} \tag{6}$$

According to the interpolation method [42], the robot can finish the rotation planning to aim in the targeted direction when the robot body moves from $\boldsymbol{P}_{\text{b1}}$ to $\boldsymbol{P}_{\text{b2}}$ and the tiptoe moves from $\boldsymbol{P}_{\text{tipi}}$ to $\boldsymbol{P}'_{\text{tipi}}$ $(i = 1, 2, 3, 4, 5, 6)$.

3.2. Dynamic modeling of the robot-rock combination system

After aiming, the movement process of the robot-rock combination system can be divided into three phases by four key frames (Fig. 11). More specifically:

Phase 1: The tiptoes of the rear legs kick the hacks for a distance of d_k, and the robot moves from frame 1 to 2.

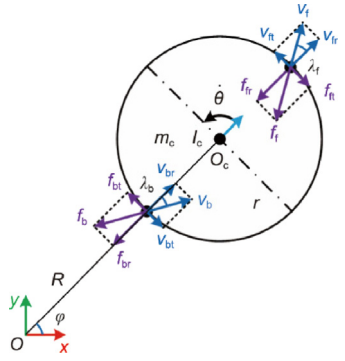

Fig. 11. The sliding model of the curling rock.

Phase 2: The combination system slides together along the fixed direction under the action of friction, and the robot enters frame 3.

Phase 3: The front legs push the curling rock for a distance of d_p, and the robot enters frame 4.

A 7-order polynomial interpolation is used to generate the real-time positions of the robot body and the curling rock (during phases 1 and 3) in the targeted direction. More specifically, the real-time positions, q_{int}, can be obtained by Eq. (7):

$$\begin{aligned} q_{\text{int}} = {} & c_0 + c_1(t - t_0) + c_2(t - t_0)^2 + c_3(t - t_0)^3 + c_4(t - t_0)^4 \\ & + c_5(t - t_0)^5 + c_6(t - t_0)^6 + c_7(t - t_0)^7 \end{aligned} \tag{7}$$

The coefficients can be written as follows:

$$\begin{cases} [c_0 \quad c_1 \quad c_2 \quad c_3] = \left[q_0 \quad v_0 \quad \frac{a_0}{2} \quad \frac{j_0}{6}\right] \\ c_4 = \frac{(210h - T((30a_0 - 15a_1)T + (4j_0 + j_1)T^2 + 120v_0 + 90v_1))}{6T^4} \\ c_5 = \frac{(-168h + T((20a_0 - 14a_1)T + (2j_0 + j_1)T^2 + 90v_0 + 78v_1))}{2T^5} \\ c_6 = \frac{(420h - T((20a_0 - 39a_1)T + (4j_0 + 3j_1)T^2 + 216v_0 + 204v_1))}{6T^5} \\ c_7 = \frac{(-120h + T((12a_0 - 12a_1)T + (j_0 + j_1)T^2 + 60v_0 + 60v_1))}{6T^7} \\ [T \quad h] = [t_1 - t_0 \quad q_1 - q_0] \end{cases} \tag{8}$$

where $q_0, q_1, v_0, v_1, a_0, a_1, j_0, j_1, t_0$, and t_1 are respectively the position, velocity, acceleration, jerk, and time at the start or end moment, and t is the current time. The T and h are the interpolation interval time and position. The boundary conditions can be obtained by the following:

$$\begin{bmatrix} q_0 & q_1 \\ v_0 & v_1 \\ a_0 & a_1 \\ j_0 & j_1 \\ t_0 & t_1 \end{bmatrix} = \begin{bmatrix} 0 & d_k \text{ or} d_p \\ 0 & v_k \text{ or} v_p \\ 0 & 0 \\ 0 & 0 \\ 0 & 2q_1/v_1 \end{bmatrix} \tag{9}$$

where v_k and v_p are the kicking and pushing velocities at the end moment.

The acceleration $a_{cs}(k)$ and velocity $v_{cs}(k)$ of the combination system during phase 2 at the kth moment can be written as follows:

$$\begin{cases} (m_r + m_c)a_{cs}(k) = -\mu_r m_r g - \mu_c m_c g \\ v_{cs}(k) = v_k + \sum_{i=0}^{k} a_{cs}(i)\Delta T \end{cases} \tag{10}$$

where u_r, u_c, m_r, and m_c are the friction coefficients and masses of the robot and curling rock, respectively; and g and ΔT are the gravity acceleration and sample interval, respectively.

The real-time velocities of the robot and the curling rock during phase 3 can be calculated using the conservation of energy. The total energy of the combined system $(E_v(t))$ at time $k-1$ is

$$E_v(k-1) = \frac{m_r v_r(k-1)^2}{2} + \frac{m_c(v_r(k-1) + v_{rc}(k-1))^2}{2} \tag{11}$$

where v_r is the robot velocity, v_{rc} is the velocity of the curling rock relative to the robot, and $v_{rc}(k-1)$ is equal to $v_p(k-1)$.

The energy consumed by friction ($E_f(k)$) from time $k-1$ to k is

$$E_f(k) = -\frac{\mu_r m_r g(v_r(k-1)+v_r(k))\Delta T}{2} - \frac{\mu_c m_c g(v_r(k-1)+v_{rc}(k-1)+v_r(k)+v_{rc}(k))\Delta T}{2} \quad (12)$$

The total energy of the combined system at time k is

$$E_v(k) = \frac{m_r v_r(k)^2}{2} + \frac{m_c(v_r(k)+v_{rc}(k))^2}{2} \quad (13)$$

According to the conservation of energy at $k-1$ and k, we have

$$E_v(k) = E_v(k-1) + E_f(k) \quad (14)$$

Now, we can substitute Eqs. (11), (12), and (13) into Eq. (14), and the robot velocity can be written as follows:

$$\begin{cases} p_1 = \frac{(m_r+m_c)}{2} \\ p_2 = m_c v_{rc}(k) + 0.5\mu_r m_r g\Delta T + 0.5\mu_c m_c g\Delta T \\ p_3 = 0.5m_c v_{rc}(k)^2 - 0.5m_r v_r(k-1)^2 - 0.5m_c(v_r(k-1)+v_{rc}(k-1))^2 \\ \quad +0.5\mu_r m_r g v_r(k-1)\Delta T + 0.5\mu_c m_c g(v_r(k-1)+v_{rc}(k-1)+v_{rc}(k)) \\ v_r(k) = \frac{-p_2+\sqrt{p_2{}^2-4p_1p_3}}{2p_1} \end{cases} \quad (15)$$

The velocity of the curling rock can be written as follows:

$$v_c(k) = v_r(k) + v_{rc}(k) \quad (16)$$

3.3. Modeling the sliding of the curling rock

Here, we propose a sliding model to analyze the movement trajectory of the curling rock. As shown in Fig. 11, the curling rock slides on the ice sheet with a linear velocity $\dot{R}$ in the φ direction, a rotation velocity $\dot{\theta}$, and a revolution velocity $\dot{\varphi}$. The plane of $\varphi+\frac{\pi}{2}$ passes through the center of the curling rock, dividing the curling rock into the front and the back parts. Each part has a mass of $\frac{m_c}{2}$ and the friction coefficients are μ_f and μ_b, respectively.

We assume that the mass of half a curling rock is concentrated in the intersection of the running band and the forward direction (φ direction). The velocities of the front and back parts in the φ direction (v_{fr} and v_{br}) are both equal to $\dot{R}$, while the velocities (v_{ft} and v_{bt}) in the lateral direction (the $\varphi+\frac{\pi}{2}$ direction) can be written as follows:

$$\begin{cases} v_{ft} = R\dot{\varphi} + r\left(\dot{\theta}+\dot{\varphi}\right) \\ v_{bt} = R\dot{\varphi} - r\left(\dot{\theta}+\dot{\varphi}\right) \end{cases} \quad (17)$$

The angles between the forward and lateral velocities of the front and back parts (λ_f and λ_b) are respectively written as follows:

$$\begin{cases} \lambda_f = \frac{R\dot{\varphi}+r\left(\dot{\varphi}+\dot{\theta}\right)}{\dot{R}} \\ \lambda_b = \frac{R\dot{\varphi}-r\left(\dot{\varphi}+\dot{\theta}\right)}{\dot{R}} \end{cases} \quad (18)$$

The frictions of the front and back parts (f_f and f_b) are respectively written as follows:

$$\begin{cases} f_f = \frac{\mu_f m_c g}{2} \\ f_b = \frac{\mu_b m_c g}{2} \end{cases} \quad (19)$$

The frictions of the front and back parts can be further decomposed into forward (f_{fr} and f_{br}) and lateral friction (f_{ft} and f_{bt}), as follows:

$$\begin{cases} f_{fr} = f_f \cos\lambda_f \\ f_{ft} = f_f \sin\lambda_f \\ f_{br} = f_b \cos\lambda_b \\ f_{bt} = f_b \sin\lambda_b \end{cases} \quad (20)$$

The dynamic equation of the curling rock sliding can be written as follows:

$$\begin{cases} I_c\ddot{\theta} = -(f_{ft}+f_{bt})rm_c a_t = f_{bt} - f_{ft} m_c a_r = -f_{br} - f_{fr} \end{cases}. \quad (21)$$

where $\ddot{\theta}$, I_c, a_t, and a_r are the rotation acceleration, moment of inertia, lateral acceleration, and forward linear acceleration of curling rock, respectively.

4. Model analyzing and matching

In this section, the relationship between the above models and actual robot control system is established. First, the influences of all parameters on the curling trajectory in these models are systematically analyzed. Most of the secondary parameters are set to fixed values, and the key parameters—including the kicking velocity, pushing velocity, and aiming direction—are set to variable values. Second, since the duration of one throw is short, the friction state between the ice and the curling rock (the equivalent friction coefficient and ratio of the back and front rock) is considered to remain the same and is estimated by means of model matching. Next, the pivotal three parameters inputted into robot controller are determined by searching based on the friction. Finally, the actual friction is modified according to the historical throwing errors.

4.1. Influences of parameters on the movement of the curling rock

The velocity at the end of phase 3 (v_{c3}) is the initial velocity $\dot{R}$ of the above sliding model that determines the forward displacement and the curling distance while the v_{r3} is the corresponding velocity of robot. The kicking velocity v_k, the duration time t_{p2} of phase 2, and the pushing velocity v_p are three input parameters in the throwing task. The duration time t_{p1} and t_{p3} of phase 1 and phase 3 can be obtained by the corresponding velocities and distances in Eq. (9). A series of typical parameters are listed in Table 1, and the corresponding velocities of the robot and curling rock are shown in Fig. 12. Their energies at certain critical time points are listed in Table 2, where E_{cs1}, E_{c3}, E_{r3}, E_{cs3}, ΔE_{cs3}, and η are the total energy of the combined system at the end of phase 1, the energy of the curling rock before its separation from the robot, the energy of the robot before separation, the total energy of the combined system before separation, the lost energy of the combined system before separation, and the throw efficiency ($\frac{E_{c3}}{E_{cs1}}$). In Fig. 12, curves 1, 2, and 3 have the same kicking velocities and duration time in phase 2 but different pushing velocities. Thus, the curves remain the same in phases 1 and 2. However, they have different duration times in phase 3, where the time increases as the pushing velocity decreases. Curve 2 has the longest time, t_{p3}, and the longest sliding distance; thus, its lost energy before full separation is the maximum of 9.3984 J, which is consistent with the lowest efficiency of 33.58%. Compared with curves 1, 2, and 3, curves 4, 5, and 6 have a longer duration time in phase 2, resulting in a longer sliding distance in phase 2, which decreases the efficiency. The duration time of phase 2 is a relatively secondary factor for the velocity of the robot and the curling rock, since the velocity of v_{c3} only decreases by 0.03 m·s^{-1}. Curves 1, 7, and 8 have different kicking velocities but the same pushing velocities and duration time in phases 2 and 3; more energy is lost and the efficiency is lower in curve 8, which has a higher kicking velocity that leads to a longer sliding distance before separation. In the actual robot controller, t_{p2} is fixed as 0.3 s, and the pivotal throwing velocity v_{c3} is adjusted by the major factors, including the kicking and pushing velocities.

Our sliding model in Section 3.3 is an intuitive model rather than an original model, but it still fits the measured trajectories

Table 1
Velocities of the robot and curling rock at the end of phase 3 with different input parameters.

Number	$v_k(\mathrm{m\cdot s^{-1}})$	$v_p(\mathrm{m\cdot s^{-1}})$	$v_{c3}(\mathrm{m\cdot s^{-1}})$	$v_{r3}(\mathrm{m\cdot s^{-1}})$	t_{p1}(s)	t_{p2}(s)	t_{p3}(s)
1	1.8	0.9	2.4210	1.5211	0.7222	0.3	0.4444
2	1.8	0.7	2.2733	1.5733	0.7222	0.3	0.5714
3	1.8	1.1	2.5626	1.4628	0.7222	0.3	0.3636
4	1.8	0.9	2.3908	1.4909	0.7222	0.6	0.4444
5	1.8	0.7	2.2434	1.5435	0.7222	0.6	0.5714
6	1.8	1.1	2.5321	1.4323	0.7222	0.6	0.3636
7	1.6	0.9	2.2155	1.3156	0.8125	0.3	0.4444
8	2.0	0.9	2.6253	1.7254	0.6500	0.3	0.4444

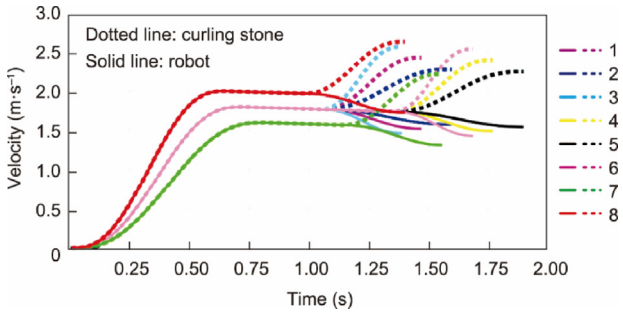

Fig. 12. Velocity curves of the robot and curling rock with different input parameters.

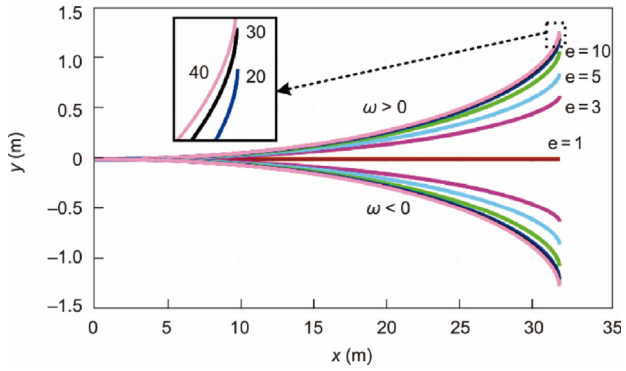

Fig. 13. The calculated trajectory of the curling phenomenon under different ratios e and rotation directions.

and predicts the trajectories well after parameter matching. There are three vital parameters to determine the calculated trajectory with the same initial velocity of the curling rock, v_{c3}, after throwing: the ratio e of the friction coefficients of the back and front rock ($\frac{\mu_b}{\mu_f}$), the equivalent friction coefficient μ_{equ}, and the initial angular velocity ω.

First, in order to be consistent with the curling phenomenon, the ratio e needs to be adjusted to generate the correct deflection direction and amplitude of the trajectory. More specifically, for a curling rock with a counterclockwise rotation (Fig. 11), the lateral friction of the back part (f_{bt}) will be greater than that of the front part (f_{ft}) if the ratio $e > 1$. Then, the direction of the lateral acceleration of the curling rock in Eq. (21) will be consistent with the direction of f_{bt}, which means that the trajectory of the curling rock will deviate to the left. It should be noted that, if the ratio $0 < e < 1$, the direction of the trajectory deviation will be against the curling phenomenon. If the ratio $e = 1$, the curling phenomenon will disappear. A trajectory with a different e and rotation direction under v_{c3} = 2.5 m·s^{-1}, $|\omega|$ = 30 r·min^{-1}, and $\mu_{equ} = 0.01$ is shown in Fig. 13. The curling distance is positively related to the ratio e, and the closer e is to 1, the higher the rate of changes will be. This phenomenon is well understood because, when e is close to 1 and changes a little, the front and rear friction coefficients will change greatly, whereas when e is much greater, even if e changes greatly, the front friction coefficient will always be close to zero and the rear one will be close to 0.02. According to the observed results in the measured trajectories, the actual curling distances are around 1–1.3 m. Then, we can estimate that the value of e approximately fluctuates between 10 and 40.

The second parameter in the sliding model of the curling rock is the equivalent friction coefficient, which can be written as follows:

$$\mu_{equ} = \frac{\mu_f + \mu_b}{2} \tag{22}$$

The relationships between the friction coefficients of each part and the equivalent coefficient can be obtained by

$$\begin{cases} \mu_f = \frac{2\mu_{equ}}{e+1} \\ \mu_b = \frac{2e\mu_{equ}}{e+1} \end{cases} \tag{23}$$

Fig. 14 shows the calculated trajectories of a curling rock with different equivalent coefficients under the same conditions of v_{c3} = 2.5 m·s^{-1}, $|\omega|$ = 30 r·min^{-1}, and e = 1 or 30. A greater μ_{equ} leads to shorter sliding and curling distances. There is a nonlinear relationship between the forward sliding distance and μ_{equ}: the change rate of the distance is lower when μ_{equ} is greater.

Lastly, the direction and amplitude of the initial rotation velocity of the curling rock have significant impacts on the curling

Table 2
Energy values of the combined system at critical time points.

Number	E_{cs1}(J)	E_{c3}(J)	E_{r3}(J)	E_{cs3}(J)	ΔE_{cs3}(J)	η
1	153.9	58.6124	86.7654	145.3778	8.5222	38.08%
2	153.9	51.6789	92.8227	144.5016	9.3984	33.58%
3	153.9	65.6692	80.2419	145.9111	7.9889	42.67%
4	153.9	57.1592	83.3544	140.5136	13.3864	37.14%
5	153.9	50.3284	89.3397	139.6681	14.2319	32.70%
6	153.9	64.1153	76.9306	141.0459	12.8541	41.66%
7	121.6	49.0844	64.9051	113.9895	7.6105	40.37%
8	190	68.9220	111.6377	180.5597	9.4403	36.27%

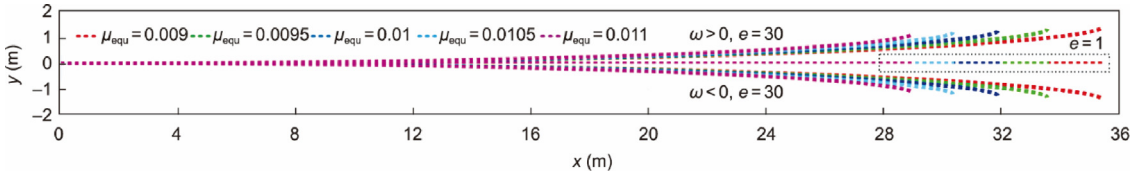

Fig. 14. Calculated trajectories of the curling rock with different ratios e and equivalent friction coefficients μ_{equ}.

trajectory. Calculated trajectories with different initial ω are illustrated in Fig. 15 under the same conditions of v_{c3} = 2.5 m·s^{-1} and e= 30. The initial ω only has a great influence on the curling distance, not on the forward distance. According to the experience of curling coaches, the curling rock should rotate 3–4 turns from separation to stopping. To conform to experience and reduce the number of variables, the initial ω is set as 30 rpm because the radius ratio of the curling rock and the driving wheel is 2.2.

4.2. Model matching

The calculated trajectory of the curling rock must be matched with the measured trajectory. The key strategy is to adjust the ratio e to obtain the actual curling distance and estimate the equivalent friction coefficient to control the forward displacement, which can be obtained by the following equation:

$$\mu_{equ} = \frac{{v_{c3}}^2}{2gl} \tag{24}$$

where l is the total length of the measured trajectory.

As illustrated in Fig. 16, a series of measured trajectories (ten experiments) is marked by dotted lines when the curling rock is thrown along the central axis of the curling sheet ($\theta_c = 0^\circ$) with different initial velocities, so the actual curling distance, which is the distance bias from the stopping point to the central axis, can be easily measured. Detailed information on the corresponding trajectory is listed in Table 3. The initial velocity v_{c3} at the moment of separation is about 2.3–2.5 m·s^{-1}. The actual friction coefficient has a great influence on the actual forward and curling distances. The corresponding equivalent friction coefficient is estimated using Eq. (24), and the friction coefficients of different parts with different ratios e can be obtained from Eq. (23). The error of the stopping points in the calculated and measured trajectories is recorded; it will be less than the radius (0.15 m) of the smallest white disc in the house if $e = 30$ in all throwing tasks. The calculated trajectories with $e = 30$ are further marked by solid lines in Fig. 17 and coincide well with the measured trajectory.

4.3. Determining parameters

The actual measured trajectory of the curling rock is determined by the following parameters: the kicking velocity v_k, duration time t_{p2}, pushing velocity v_p, initial rotating velocity ω, initial aiming direction θ_c, friction coefficient μ_{equ}, and ratio e. The duration time and rotating velocity are set permanently as 0.3 s and 30 rpm, respectively, to reduce the number of variables. The real friction coefficient is time-varying and is initially set as 0.01, which is a typical value on a fresh ice sheet as reported in other papers [3,11,43]. The initial ratio e is set as 30, which is reasonable according to the matching analysis in Section 4.2. A series of trajectories is calculated with small intervals to determine the optimal parameters, including v_k, v_p and θ_c. Fig. 17 illustrates the searching results with fixed intervals of 0.05 m/s, 0.05 m/s, and 0.1°. The evaluation index is the radius of the circle that is calculated by the reciprocal of the distance error between the stopping point in the calculated trajectory and the targeted point $\boldsymbol{P}_t$ from the visual system, so the corresponding parameters of the circle with the maximum radius are optimal. Figs. 17(a) and (b) are the searching results when the curling rock is thrown to the center of the house with an initial $\omega = 30$rpm and -30 rpm, while Figs. 17(c) and (d) are the corresponding results to reach a general targeted point $[38.61 \ -0.563]^T$. In each part of the figure, the picture on the right side shows the vertical view of the $v_k - v_p$ plane. The calculated trajectories using the searching results for optimal parameters in Fig. 17 are shown in Fig. 18. For each targeted point in the throwing task, there are two symmetric trajectories about the line between the start and end points of the trajectory with the opposite initial rotating velocities and the same velocities v_k and v_p, respectively. More specifically, the trajectories in (a) and (b) are symmetric about the line in direction 0°, while trajectories (c) and (d) are symmetric about the line in direction –0.85°.

4.4. Model adjusting method

The real friction between the curling rock and the ice sheet is unknown at the beginning of the throw, and the initial values of the parameters of the sliding model can only be obtained through experience. The error between the actual and estimated parameters should be corrected according to the results for the previous throw. More specifically, the initial independent parameters, μ_{equ} and e, are set as 0.01 and 30, respectively, for the first throw. Then, the dependent parameters—that is, the kicking velocity v_k, pushing velocity v_p, and initial aiming direction θ_c—can be determined using the searching method given in Section 4.3. Two classical PI controllers are used to correct the errors in the sliding and curling distances.

The initial position of the curling rock before kicking can be written as follows:

$$^{w}\boldsymbol{P}_{c1} = \boldsymbol{R}_z(\theta_c) \ {}^{b}\boldsymbol{P}_{c1} + {}^{w}\boldsymbol{P}_{b} \tag{25}$$

where ${}^{b}\boldsymbol{P}_{c1}$ is the position vector from the center of the robot body to the curling rock in the body coordinate system and ${}^{w}\boldsymbol{P}_{b}$ is the body position in the world coordinate system, which is given by the vision system. $\boldsymbol{R}_z(\cdot)$ is the rotation matrix around axis z. The error in the sliding distance $\widetilde{l}_t$ can be estimated as follows:

$$\widetilde{l}_t = \|{}^{w}\boldsymbol{P}_{cd2} - {}^{w}\boldsymbol{P}_{c1}\|_2 - \|{}^{w}\boldsymbol{P}_{ca2} - {}^{w}\boldsymbol{P}_{c1}\|_2 \tag{26}$$

where ${}^{w}\boldsymbol{P}_{cd2}$ and ${}^{w}\boldsymbol{P}_{ca2}$ are respectively the desired and actual stopping positions of the curling rock in the world coordinate system.

The curling distance cannot be measured directly using the model matching method (Section 4.2) because of the nonzero initial direction bias of θ_c; however, the measurement can be finished in the initial robot coordinate frame after the direction adjustment. The error of the curling distance $\widetilde{l}_c$ can be calculated as follows:

$$\widetilde{l}_c = \left({}^{w}\boldsymbol{P}_{cd2} - {}^{w}\boldsymbol{P}_{ca2} \right)^T \cdot \left(\boldsymbol{R}_z(\theta) \begin{bmatrix} 0 \\ 1 \\ 0 \end{bmatrix} \right) \tag{27}$$

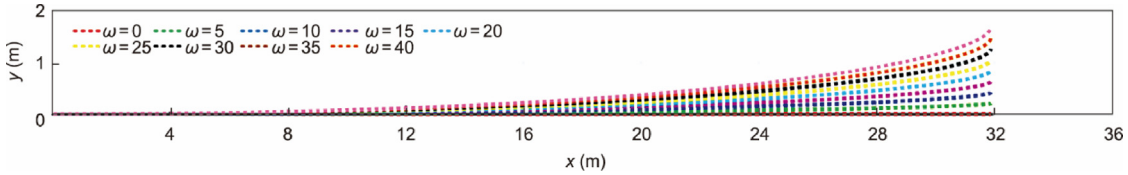

Fig. 15. Calculated trajectories of the curling rock with different initial rotation velocities.

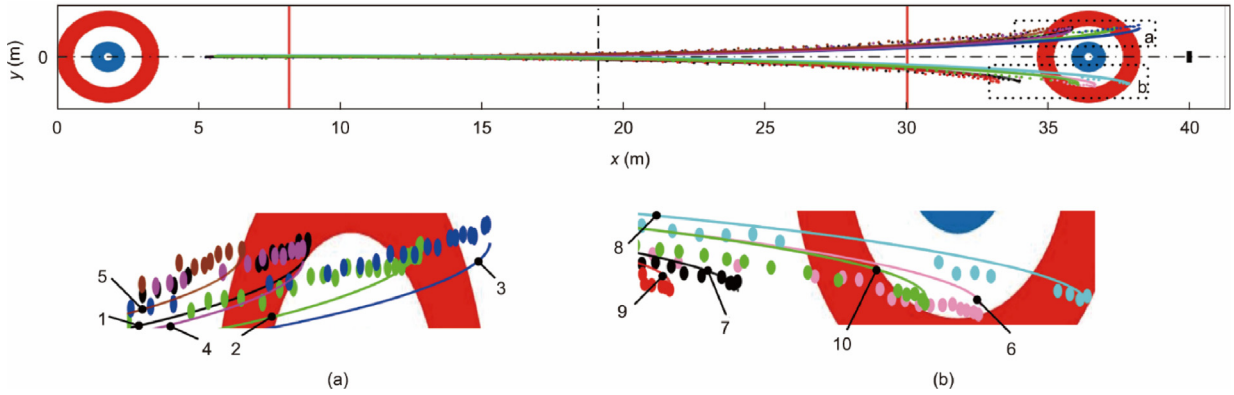

Fig. 16. Calculated trajectories (solid line) and measured trajectories (dotted line) of the curling rock with $\theta_c = 0^\circ$.

Table 3
Key information on the measured and calculated trajectories in 10 throw tasks along the center axis.

Number	$v_{c3}\,(\mathrm{m}\cdot\mathrm{s}^{-1})$	Forward distance	Curling distance	μ_{equ}	Error (e = 2)	Error (e = 5)	Error (e = 10)	Error (e = 20)	Error (e = 30)	Error (e = 40)
1	2.318	29.98	1.17	0.0091	0.802	0.406	0.209	0.091	0.048	0.026
2	2.372	31.33	1.09	0.0092	0.720	0.315	0.114	0.014	0.053	0.076
3	2.513	33.01	1.28	0.0098	0.901	0.493	0.290	0.168	0.124	0.101
4	2.482	30.40	1.14	0.0103	0.792	0.415	0.227	0.114	0.073	0.241
5	2.409	29.48	1.08	0.0100	0.732	0.356	0.168	0.056	0.016	0.051
6	2.444	31.28	1.19	0.0097	0.827	0.432	0.235	0.117	0.074	0.007
7	2.499	28.77	0.93	0.0111	0.607	0.253	0.077	0.032	0.069	0.052
8	2.462	32.20	1.09	0.0096	0.720	0.317	0.117	0.013	0.050	0.089
9	2.452	27.43	1.00	0.0112	0.691	0.350	0.181	0.079	0.042	0.072
10	2.500	30.50	1.11	0.0105	0.763	0.201	0.201	0.088	0.047	0.022

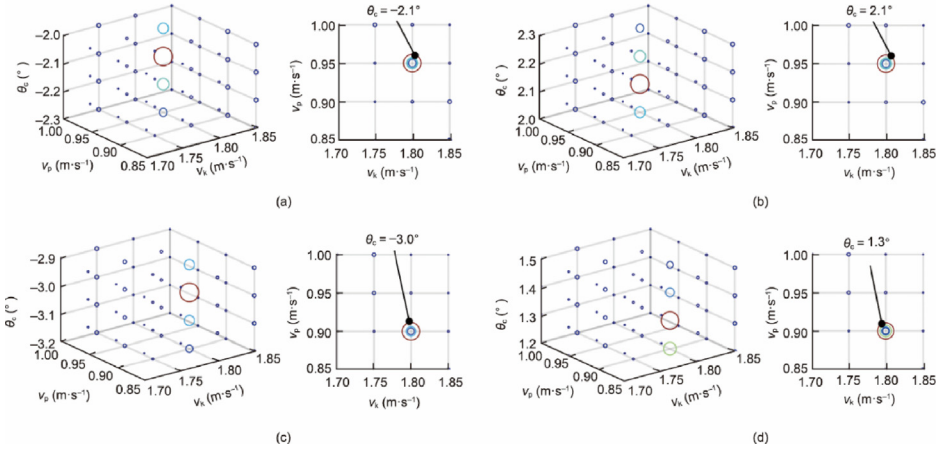

Fig. 17. Searching results for optimal parameters with fixed intervals.

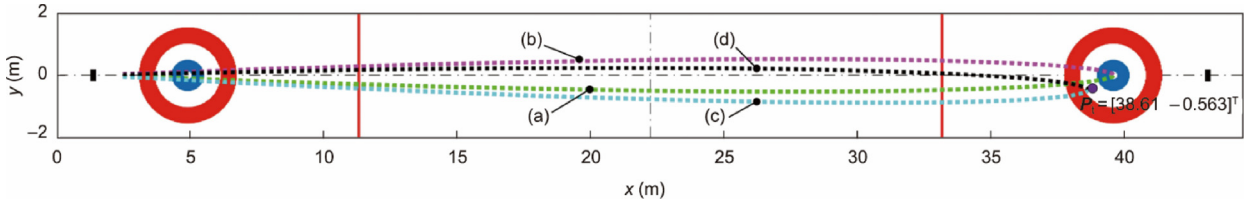

Fig. 18. The calculated trajectory with corresponding optimal parameters.

The independent parameters in the kth experiment ($k \geq 2$) are adjusted as follows:

$$\begin{cases} \mu_{\text{equ}}(k) = K_{\text{p}\mu}\tilde{l}_{\text{t}}(k-1) + K_{\text{i}\mu}\sum_{i=1}^{k-1}\tilde{l}_{\text{t}}(k-1) + \mu_{\text{equ}}(k-1) \\ e(k) = K_{\text{pe}}\tilde{l}_{\text{c}}(k-1) + K_{\text{ie}}\sum_{i=1}^{k-1}\tilde{l}_{\text{c}}(k-1) + e(k-1) \end{cases} \tag{28}$$

where $K_{\text{p}\mu}$, $K_{\text{i}\mu}$, K_{pe}, and K_{ie} are the proportional and integral gains of μ_{equ} and e, respectively.

5. Simulation and experiment

5.1. Simulation

Five groups of simulations, with 10 times in each group, were performed using the above method to analyze the convergence when throwing the curling rock to the targeted points. As shown in Fig. 19(a), four points evenly distributed on the outer edge of the blue circle and the center of the circular region were chosen as the targeted stopping points in each group of simulations and are denoted by a star. The actual stopping points are denoted by circles. The parameters are listed in Table 4; the actual friction coefficient μ_{equ} and ratio e were set as 0.01 and 25 in all simulations. An initial clockwise rotating velocity (ω_{init}) of 30 r·min^{-1} was used to generate a throw that curves to the right, and vice versa. There were biases of ±10% and ±20% for the estimated parameters of μ_{equ} and e in the first simulation. The distance error between the targeted and actual stopping points is illustrated in Fig. 19(b); it is larger than zero when the estimated μ_{equ} is smaller than the actual one in simulations 1 and 2, and vice versa in simulations 3, 4, and 5. The absolute error quickly converges to 0.7 m in the third simulation from 3.6 m, and then slowly decreases to the stable absolute error of 0.2 m. It should be noted that the stable error in the simulation can be further reduced by narrowing the searching interval in Section 4.3; however, the searching time will increase by a cubic power. Thus, the intervals of v_{k}, v_{p}, and θ_{c} are set as 0.025 m·s^{-1}, 0.025 m·s^{-1}, and 0.1° in all simulations and experiments for a tradeoff between error and efficiency. The radius of the error circle in each group is shown using a box graph in Fig. 19(c), where the two finite outliers are from the first two throwing simulations in each group. The maximum bias between the 25th and 75th percentile is from 0.113 to 0.693 m in the fourth simulation group, whereas the minimum bias is from 0.111 to 0.403 m in the fifth group. The convergence process of the trajectory in the first five simulations in the first group is illustrated in Fig. 20.

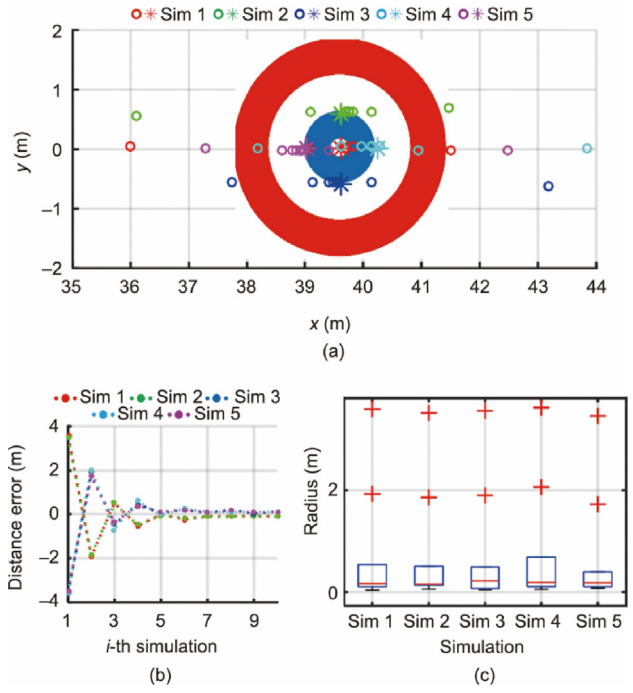

Fig. 19. Simulation results: (a) Targeted stopping points are denoted by stars and actual stopping points are denoted by circles, (b) The distance error between the targeted and actual stopping points, (c) The radius distribution from the targeted stopping point to the actual stopping point. Sim: simulation.

During the experiment, the robot walks on the ice sheet in a six-legged state and crawls in a four-legged state when throwing the rock. After completing a throw, the robot must return to the vicinity of the hack in a six-legged state, and then change to a four-legged state for the next throw. The cycle of the throwing process is shown in Fig. 21. First, the robot is in a six-legged state (Fig. 21(a)); it prepares to find the hacks (Fig. 21(b)) and switches the middle legs from the 'L' to 'anti-L' configuration in order to position the CoM within the support polygon consisting of the middle and rear legs (Fig. 21(c)). Then, it switches the front legs from the vertical state to the horizontal grasping state (Fig. 21(d)); it reduces its height and puts the rear legs on the hack (Fig. 21(e)). Next, the robot adjusts the aiming direction with the support of the rear and middle legs (Fig. 21(f)). It rotates the middle legs to the rear to support the body, together with the plastic cylinders mounted on the front legs (Fig. 21(g)). The robot kicks the hacks with its rear legs to accelerate (Fig. 21(h)), slides with the curling rock (Fig. 21(i)), and pushes the rock with its front legs to accelerate the curling rock again (Fig. 21(j)). After the throw, the robot's middle legs switch to the 'anti-L' configuration and support the body, with the rear legs together (Fig. 21(k)). The front legs switch to the vertical state for walking (Fig. 21(l)). Lastly, the middle legs rotate to the 'L' configuration for walking in a 3-3 gait. A detailed morphology transformation video has been provided (Video S1 in the Appendix A). The detailed throwing process is illustrated in Fig. 22. The acceleration process of the combination of the robot and curling rock can be divided into three phases, like the schematic diagram in Fig. 10. After throwing, the curling rock will slide forward with rotation under the action of friction. A classic throw to the base camp is shown in Video S2 (Appendix A).

5.1.1. Error-measurement experiment

The trajectory of the curling rock is influenced by the errors in the kicking velocity v_{k}, pushing velocity v_{p}, and orientation angle

Table 4
Model parameters in five groups of simulations.

Number	Direction	ω_{init}(r·min^{-1})	$\mu_{equ}(1)$	$e(1)$	μ_{equ}	e	Target point
Sim 1	Clockwise	−30	0.009	30	0.01	25	[39.63 0]
Sim 2	Anticlockwise	30	0.009	20	0.01	25	[39.63 0.61]
Sim 3	Clockwise	−30	0.011	30	0.01	25	[39.63 −0.61]
Sim 4	Clockwise	−30	0.011	30	0.01	25	[40.24 0]
Sim 5	Anticlockwise	30	0.011	30	0.01	25	[39.02 0]

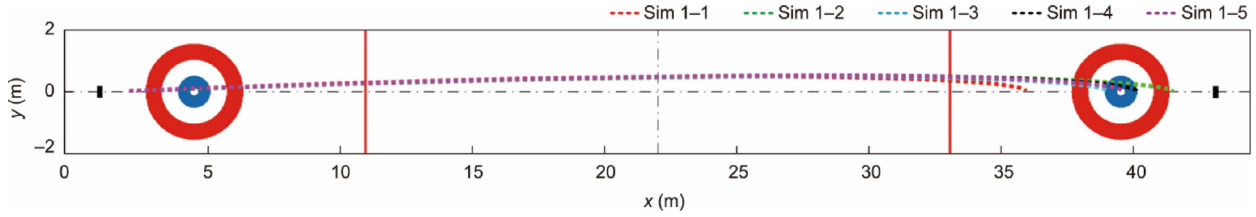

Fig. 20. Calculated trajectory of the curling rock in the first group of simulations.

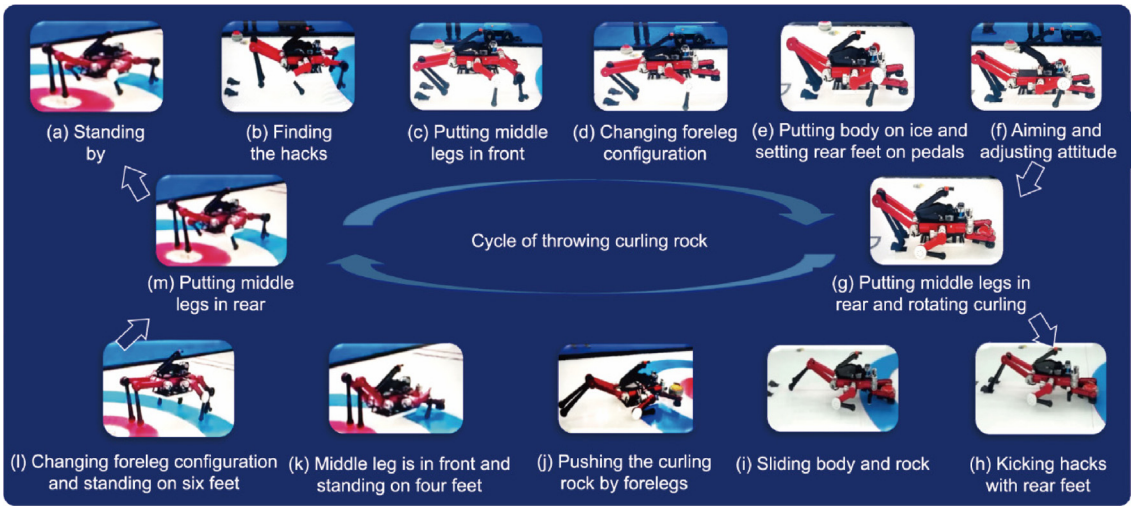

Fig. 21. The cycle of throwing a curling rock: The robot searches for the hacks in its six-legged state and throws the curling rock in its four-legged state.

θ_c, as well as by the actual friction coefficient μ_{equ} and the ratio e. The first three errors are intrinsic and dependent on the robot performance, while the rest are extrinsic and dependent on the ambient temperature, the duration time from the ice sheet laid, and the scratches on the sheet. Similar to the simulations, three key points (marked with stars) were chosen as the targeted stopping points for the three group of experiments, as shown in Fig. 23(a). In the figure, the small circles illustrate the distribution of the actual stopping points of 10 repetitive experiments in each group. The experiment conditions are listed in Table. 5. All 30 experiments used the same input parameters, including an initial clockwise angular velocity of 30 r·min^{-1}, an equivalent friction coefficient of 0.01, and a ratio of 30. Three sets of output parameters, including the kicking velocity, pushing velocity, and orientation angle, were searched for according to the method described in Section 4.3. The distance error between the targeted and actual stopping points is illustrated in Fig. 23(b). The distance error is smaller than zero when the estimated friction coefficient is greater than the actual one. The radius of the error circle in each group is shown using a box graph in Fig. 23(c); the average values were 0.798, 1.488, and 2.868 m, respectively, as determined by the bias of the estimated and actual friction coefficient. The maximum bias was from 1.312 to 3.694 m in the third group of experiments. All actual trajectories in the first group of experiments are shown in Fig. 24. The sliding distance decreased slowly with an increase in the number of experiments, owing to the increased friction coefficient that resulted from the elapsed time and the scratches produced as the experiments continued.

5.1.2. Feedback control experiment

As shown in Fig. 25(a), 10 throwing experiments toward each targeted point were further completed to test the convergence of the throwing task. The initial parameters, including the equivalent friction coefficient μ_{equ}, ratio e, and rotating velocity ω_{init}, were set as 0.01, 30, and −30 rpm, respectively. The distance errors of all three groups of experiments decreased from 2.214 m to about 1.1 m after two experiments, as shown in Fig. 25(b). The boxplot below the graph shows that most of the experiment results were concentrated within the error circle, with a maximum radius of 1.105 m (results for the third group of experiments are shown in Fig. 25(c)). Similar to the simulation results, outliers only appeared in the first few experiments and mainly resulted from the error between initial estimated friction coefficient and the actual one. A feedback controller was used to estimate the equivalent friction coefficient to converge the error; the estimated values for the k th

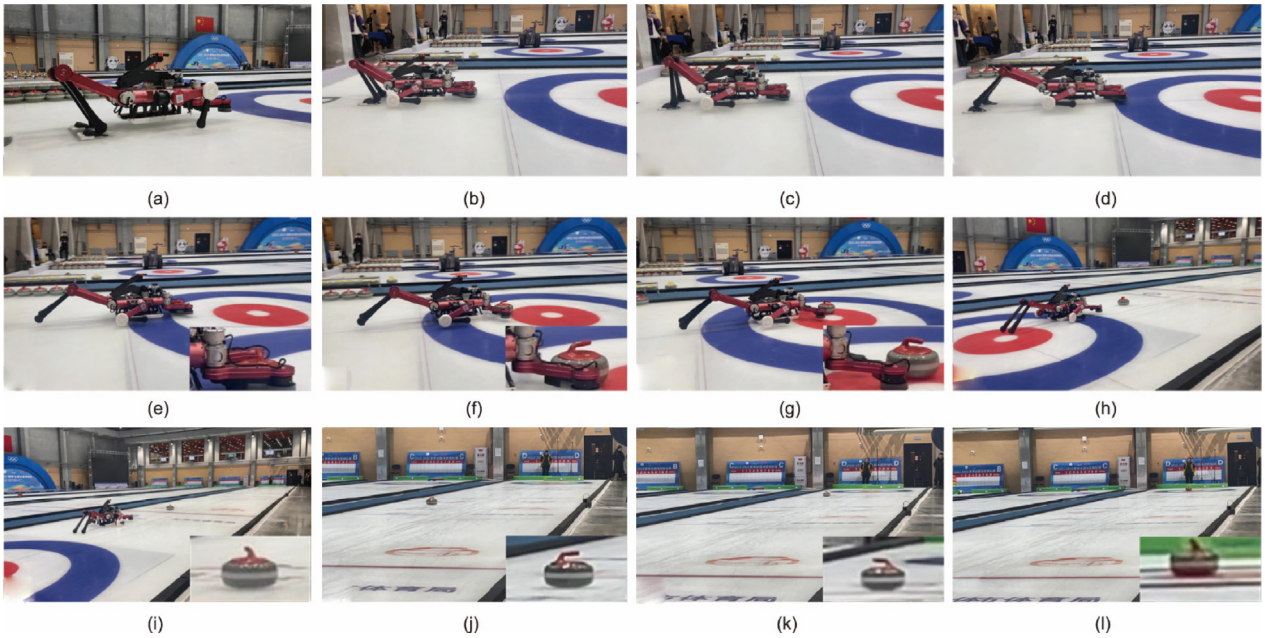

Fig. 22. Snapshots of a classic throwing experiment. (a) The middle and rear legs support the body and drive the robot to rotate around the center point of the two rear legs to aim in the target direction. (b) The front legs grab and rotate the curling rock, and the rear legs prepare to kick the hacks to speed up the body. (c) The halfway state of the rear legs kicking the hacks. (d) The ending state of the rear legs kicking the hacks and the tiptoes of the rear legs beginning to leave the hack. (e) The curling rock and the robot slide forward as a whole. (f) The halfway state of the front legs pushing the curling rock. (g) The ending state of the front legs pushing the curling rock; the curling rock separates from the robot. (h) The robot and the curling rock slide forward, separately. (i) The robot stops moving and the curling rock continues to move forward. (j) The curling rock slides into the middle of the ice sheet. (k) The curling rock moves to the back stop line. (l) The curling rock is parked in the center of the opposite base camp.

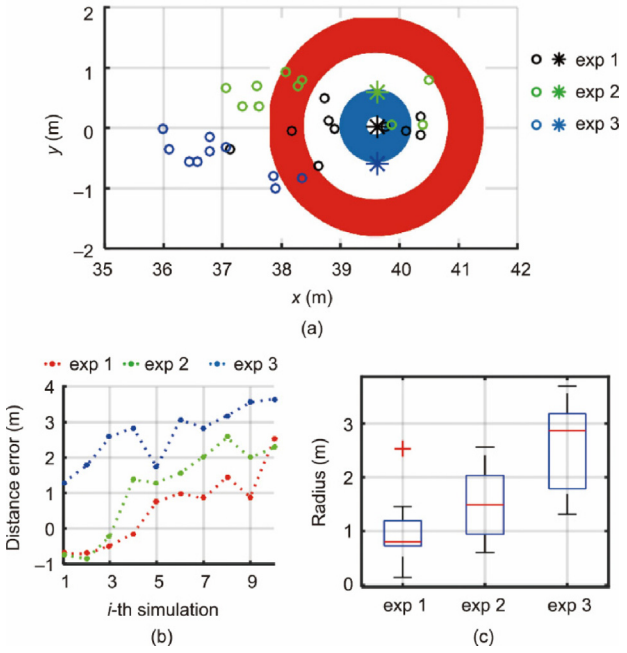

Fig. 23. Error measurement results. (a) The targeted stopping points are denoted by stars and actual stopping points are denoted by circles. (b) Distance error between the targeted and actual stopping points. (c) Radius distribution from the targeted stopping point to the actual one. exp: experiment

experiment are listed in Table 6. An increasing trend in μ_{equ} during the stable phase (after two experiments) was captured, which is consistent with the experimental results in error measurement (Section 5.2). Fig. 26 illustrates the actual trajectories in the first group of ten feedback control experiments, where the targeted point is the center of the circular region. The actual stopping points of the first few experiments were concentrated in the outer edge of the red circle with a radius of 1.83 m, while those of the last experiments were in the outer edge of the blue circle with a radius of 0.61 m.

5.1.3. Human-robot competition

To evaluate the robot's actual combat ability, we set up competitions between the curling robot and able-bodied athletes and wheelchair athletes, respectively. In accordance with the rules of official competition, each team alternately throws eight curling rocks; the final score is the number of the team's own rocks closest to the center of the circle. The actual throwing scenes are shown in Fig. 27. In the matches, the robot threw red curling rocks, while the athletes used yellow ones. The real-time progress in the two matches is illustrated in Figs. 28 and 29, where the scores are recorded in the upper-left corner of the subfigures. Match videos are also provided in Videos S3 and S4 (Appendix A). Eventually, our curling robot lost to the able-bodied athletes by two points but beat the wheelchair athletes by one point. The main reason for this difference in the competition results was that able-bodied athletes and wheelchair athletes use different methods to

Table 5
Model parameters in three group of experiments.

No.	ω_{init}(r•min^{-1})	$\mu_{equ}(k)$	$e(k)$	Target point	v_k(m•s^{-1})	v_p(m•s^{-1})	θ_c(°)
Exp. 1	−30	0.01	30	[39.63 0]	1.975	0.925	2
Exp. 2	−30	0.01	30	[39.63 0.61]	2.025	0.85	2.9
Exp. 3	−30	0.01	30	[39.63 −0.61]	2.025	0.85	1.1

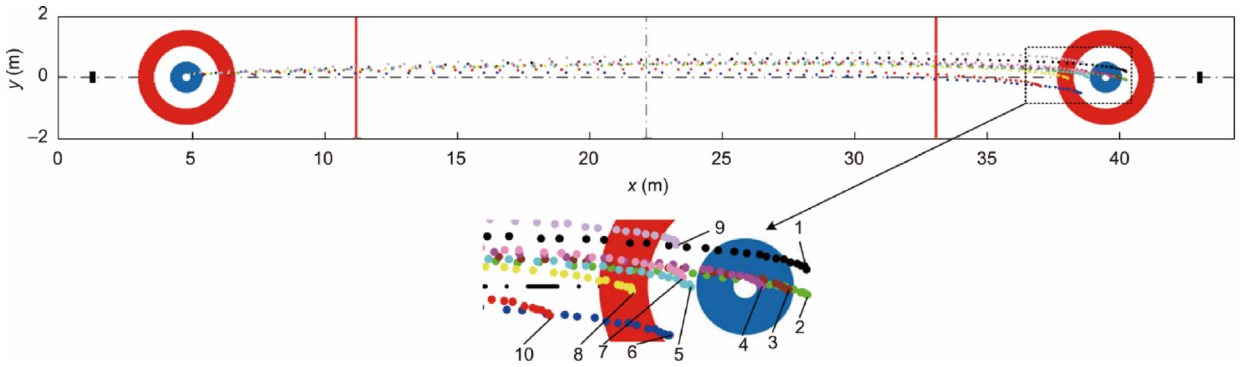

Fig. 24. Actual trajectory of the curling rock in the first group of error-measurement experiments.

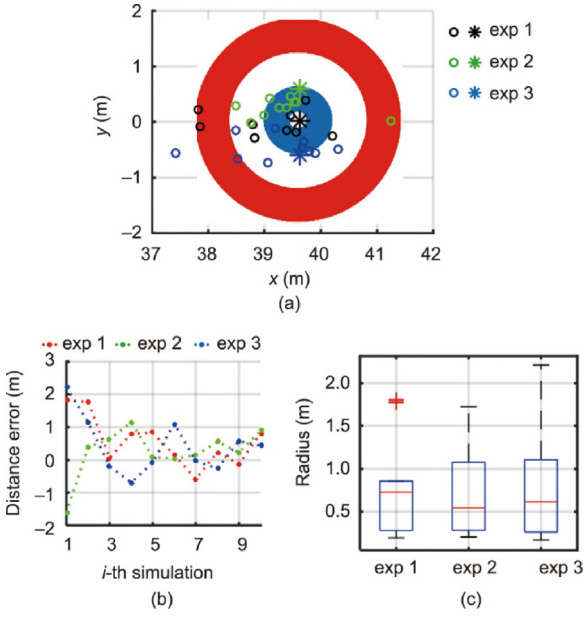

Fig. 25. Feedback control results. (a) Targeted stopping points are denoted by stars and actual stopping points are denoted by circles. (b) Distance error between the targeted and actual stopping points. (c) Radius distribution from the targeted stopping point to the actual one.

Table 6
Estimated equivalent friction coefficients of the feedback controller for the k th experiment.

k	$\mu_{equ}(k)$ in group 1	$\mu_{equ}(k)$ in group 2	$\mu_{equ}(k)$ in group 3
1	0.0100	0.0100	0.0100
2	0.0103	0.0097	0.0105
3	0.0106	0.0097	0.0108
4	0.0107	0.0098	0.0108
5	0.0108	0.0100	0.0107
6	0.0110	0.0101	0.0107
7	0.0112	0.0101	0.0110
8	0.0111	0.0101	0.0111
9	0.0112	0.0103	0.0111
10	0.0113	0.0104	0.0113

throw and control the curling rock. After the robot and wheelchair curling athletes threw the curling rock, there was no arrangement for the athletes to wipe the ice to further control the curling trajectory during the rock's movement. In contrast, the able-bodied athletes arranged another player to quickly wipe the ice to decrease the friction and enable a longer sliding distance. Hence, able-bodied players usually throw curling rocks with a relatively low velocity and further control the trajectory by wiping the ice. In future, the robot will achieve better competition results if a professional wiping robot is developed.

6. Discussion

The sliding model between the curling rock and the ice sheet plays a major role in the robot's throwing task. Both the sliding and curling distances are mainly dependent on the equivalent friction coefficient, friction ratio, and rotating velocity. However, many researchers have reported that the curling distance has a weak dependence on the rotating velocity and always deviates by about 0.9–1.2 m [3,9,11,12,44]. Our model adopts a fixed initial rotating velocity of 30 r•min^{-1} for the driving wheel in the model matching, simulation, and experiment in order to avoid the influence of rotating velocity. A model matching error of 0.124 m, shorter than the radius of the central white circle (0.15 m), is realized when the ratio e is equal to 30. It is notable that this model is an intuitive model rather than a first principles model; however, it can still quickly predict the trajectory of the curling rock and generate control parameters for the subsequent throwing experiment.

The small intervals of the searching parameters in Section 4.3 can further reduce the error in the simulation, although the searching time increases quickly at the same time. However, the decrease in error is limited by the random error of the robot system and the errors in the estimated and actual friction coefficient. The former is intrinsic and is determined by the precision of the control system, whereas the latter is extrinsic and can be modified by means of feedback control. If the random error is greater than the searching precision, shortening intervals will be fruitless, and vice versa. The actual stable error converges to 1.105 m by means of feedback control in the experiments, which is close to that of a curling athlete in a wheelchair, while the error is 0.2 m in the simulation.

7. Conclusion

In this work, a curling hexapod robot was designed and manufactured to play the sport of curling; the robot mimics human movements, including kicking, sliding, pushing, and rotating. Our curling hexapod robot is the first legged robot to succeed in the sport of curling; in comparison with existing wheeled curling robots, it has not only overcome the problems of robot slipping and ice surface damaging but also achieved excellent performance in curling throwing. The robot can complete walking and throwing tasks via morphology transformation. Two parallelogram mechanisms, where at least one mechanism always maintains a parallelogram configuration, are utilized in the leg mechanism design to

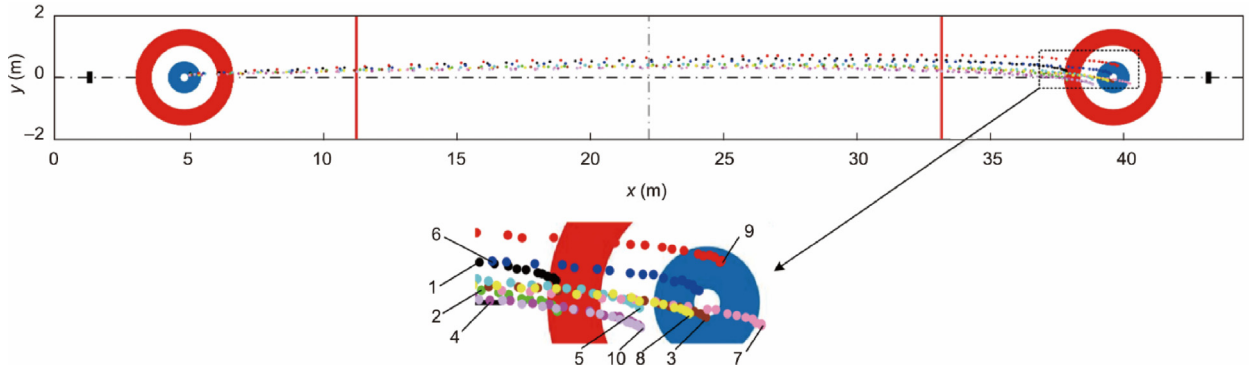

Fig. 26. Actual trajectories of the curling rock in the first group of feedback control experiments.

Fig. 27. Throwing scenes with a curling rock. (a) Two able-bodied athletes are throwing; one slides with the curling rock while the other is prepared for sweeping the ice surface with an ice broom. (b) Two wheelchair athletes are throwing; one pushes the rock with a slender rod, while the other aims at the target. (c) The hexapod curling robot is prepared for throwing.

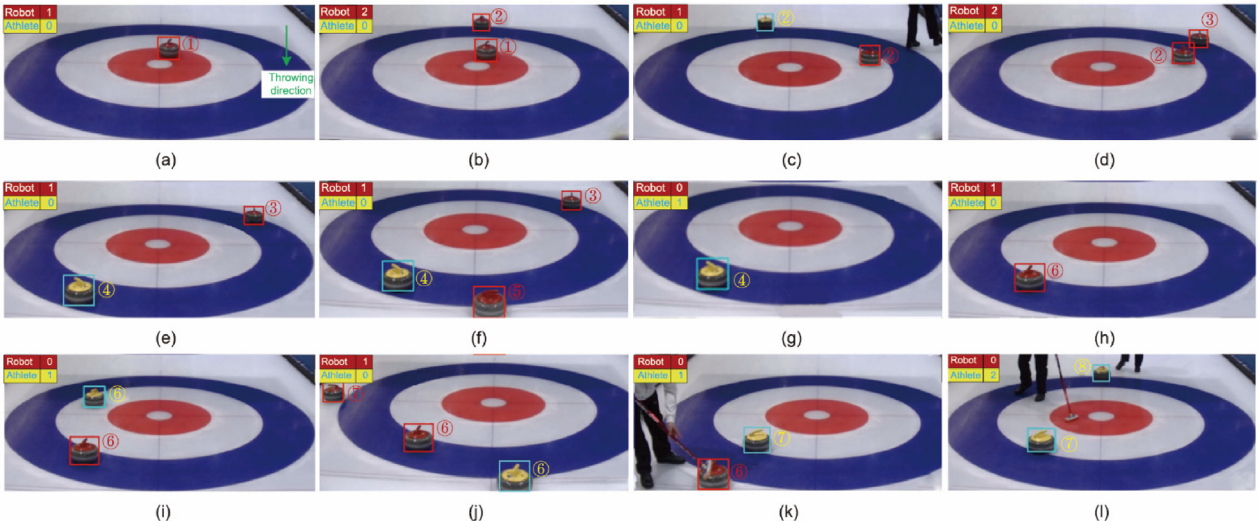

Fig. 28. Competition between the robot and able-bodied athletes. (a) The robot throws the first red curling rock into the red circle, and the athlete throws the first yellow rock outside the camp. (b) The second red rock is thrown ahead of the blue circle to guard the first red rock. (c) The second yellow rock hits the second red rock; then, the second red rock hits the first red rock, but the second red rock enters the white circle. (d) The third red rock hits the second yellow rock that then slides outside the camp, and the third red rock stops on the edge of the blue circle; next, the third yellow rock fails to hit the third red rock and slides outside the camp. (e) The fourth red rock is thrown outside the camp, and the second red rock is hit outside the camp by the fourth yellow rock, which then stops in the blue circle. (f) The fifth red rock is thrown outside the camp. (g) The third red rock is hit by the fifth yellow rock, and they all slide outside the camp. (h) The fourth yellow rock is hit outside the camp by the sixth red rock, which stops in the blue circle. (i) The sixth yellow rock is thrown into the white circle. (j) The sixth yellow rock is hit by the seventh red rock, but they all slide outside the camp. (k) The sixth red rock is hit outside the camp by the seventh yellow rock, which stops on the edge of the white circle. (l) The eighth red rock is thrown outside the camp, and the eighth yellow rock stops on the edge of the blue circle.

realize leg configuration switching. The reuse design of the robot leg achieves multiple functions, including grabbing, rotating, and pushing the curling rock, as well as supporting, accelerating, and decelerating the robot body. Models for robot aiming, the combination sliding of the robot and the curling rock, and the individual sliding of the curling rock were systematically established to predict the trajectory of the curling rock; $\mu_{equ} = 1$ and $e = 30$ were chosen as the initial input parameters for the first throw after model analysis and matching. The robot's control parameters in the throwing task, which consist of the kicking velocity v_k, pushing

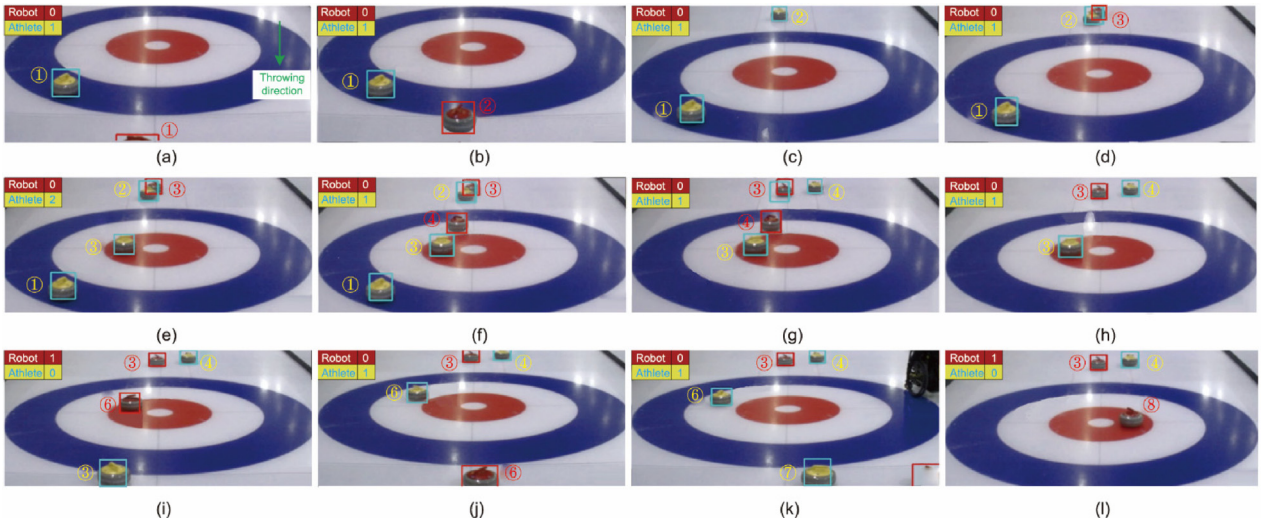

Fig. 29. Competition between the robot and wheelchair athletes. (a) The robot throws the first red curling rock outside the camp, while the wheelchair athlete throws the first yellow rock, which stops in the blue circle. (b) The second red rock stops on the edge of the blue circle. (c) The athlete throws the second yellow rock to the guard. (d) The robot also throws a guard rock (denoted by the number 3) that comes close to the second yellow one. (e) The third yellow rock is perfectly thrown into the red circle by the athlete. (f) The robot throws the fourth red rock into the white circle. (g) The fourth yellow rock hits the third red rock that hits the second yellow rock; then, the first yellow rock is hit outside the camp as well. (h) The fifth red rock is thrown outside the camp, and the fourth red rock is hit outside by the fifth yellow rock. (i) The third yellow rock is hit outside the camp by the sixth yellow rock, which perfectly stops in the red circle. (j) The sixth red rock is hit outside the camp by the sixth yellow rock, which stops in the white circle. (k) The seventh red rock fails to hit the sixth yellow rock, and the seventh yellow rock is unsuccessfully thrown outside the camp. (l) The sixth yellow rock is hit outside the camp by the eighth red rock, which stops in the red circle, and the eight yellow rock fails to hit the eighth red rock by the fourth yellow rock.

velocity v_p, and orientation angle θ_c, were determined via a searching method with intervals of v_k= 0.025 m·s^{-1}, v_p= 0.025 m·s^{-1}, and θ_c = 0.1° to ensure good precision and efficiency. In five groups of simulations, the error quickly converged from 3.6 to 0.7 m after two throwing tasks, and then slowly reached the stable error of 0.2 m thanks to the PI controller. In three groups of error measurement experiments, the error increased and diverged gradually, since the friction coefficient slowly increased in comparison with the previous throw. A feedback control experiment was further completed to adapt to environmental change based on historical errors, and a throwing error of 1.105 m was realized after two throws in all groups of experiments. Finally, the excellent performance of our robot in curling throwing was further validated through a human-robot competition.

In the future, we will study the first-principles model of the interaction between the curling rock and the ice sheet for predicting the rock trajectory. Moreover, the time consumption will be shortened to increase the efficiency by optimizing the morphology transformation.

CRediT authorship contribution statement

Feng Gao: Funding acquisition, Formal analysis, Supervision, Resources, Project administration. **Ke Yin:** Data curation, Writing – original draft, Writing – review & editing, Investigation, Validation, Formal analysis, Methodology, Software. **Yue Zhao:** Visualization. **Qiao Sun:** Visualization. **Jing Sun:** Visualization. **Xianbao Chen:** Methodology. **Yue Gao:** Supervision. **Yuguang Xiao:** Software.

Declaration of competing interest

The authors declare that they have no known competing financial interests or personal relationships that could have appeared to influence the work reported in this paper.

Acknowledgments

This work is funded by the National Natural Science Foundation of China (No. 92248303).

Compliance with ethical guidelines

Ke Yin, Yue Gao, Feng Gao, Xianbao Chen, Yue Zhao, Yuguang Xiao, Qiao Sun, and Jing Sun declare that they have no conflicts of interest or financial conflicts to disclose.

Appendix A. Supplementary material

Supplementary data to this article can be found online at https://doi.org/10.1016/j.eng.2023.10.018.

References

[1] Denny M. Curling rock dynamics. Can J Phys 1998;76(4):295–304.
[2] Denny M. Curling rock dynamics: towards a realistic model. Can J Phys 2002;80(9):1005–14.
[3] Maeno N. Curl mechanism of a curling stone on ice pebbles. Bull Glaciol Res 2010;28:1–6.
[4] Maeno N. Dynamics and curl ratio of a curling stone. Sports Eng 2014;17(1):33–41.
[5] Penner AR. The physics of sliding cylinders and curling rocks. Am J Phys 2001;69(3):332–9.
[6] Shegelski MRA, Niebergall R, Walton MA. The motion of a curling rock. Can J Phys 1996;74(9–10):663–70.
[7] Jensen ET, Shegelski MRA. The motion of curling rocks: experimental investigation and semi-phenomenological description. Can J Phys 2004;82(10):791–809.
[8] Shegelski MRA, Niebergall R. The motion of rapidly rotating curling rocks. Aust J Phys 1999;52(6):1025–38.
[9] Shegelski MRA, Lozowski E. Pivot–slide model of the motion of a curling rock. Can J Phys 2016;94(12):1305–9.
[10] Mancini G, de Schoulepnikoff L. Improved pivot–slide model of the motion of a curling rock. Can J Phys 2019;97(12):1301–8.
[11] Nyberg H, Alfredson S, Hogmark S, Jacobson S. The asymmetrical friction mechanism that puts the curl in the curling stone. Wear 2013;301(1–2):583–9.

[12] Honkanen V, Ovaska M, Alava MJ, Laurson L, Tuononen AJ. A surface topography analysis of the curling stone curl mechanism. Sci Rep 2018;8(1):8123.
[13] Kawamura T, Kamimura R, Suzuki S, Iizuka K. A study on the curling robot will match with human result of one end game with one human. In: Proceedings of 2015 IEEE Conference on Computational Intelligence and Games (CIG); 2015 Aug 31–Sep 2; Tainan, China. Piscataway: IEEE; 2015. p. 489–95.
[14] Kobilarov M, Sukhatme G, Hyams J, Batavia P. People tracking and following with mobile robot using an omnidirectional camera and a laser. In: Proceedings of 2006 IEEE International Conference on Robotics and Automation, 2006. ICRA 2006; 2006 May 15–19; Orlando, FL, USA. Piscataway: IEEE; 2006. 557–62.
[15] Kwon S, Kim S, Yu J. Tilting-type balancing mobile robot platform for enhancing lateral stability. IEEE/ASME Trans Mechatron 2015;20(3):1470–81.
[16] Kato K, Wada M. Kinematic analysis and simulation of active-caster robotic drive with ball transmission (ACROBAT-S). Adv Robot 2017;31(7):355–67.
[17] Choi JH, Nam K, Oh S. High-accuracy driving control of a stone-throwing mobile robot for curling. IEEE Trans Autom Sci Eng 2022;19(4):3210–21.
[18] Choi JH, Song C, Kim K, Oh S. Development of stone throwing robot and high precision driving control for curling. In: Proceedings of 2018 IEEE/RSJ International Conference on Intelligent Robots and Systems (IROS); 2018 Oct 1–5; Madrid, Spain. Piscataway: IEEE; 2018. p. 2434–40.
[19] Won DO, Müller KR, Lee SW. An adaptive deep reinforcement learning framework enables curling robots with human-like performance in real-world conditions. Sci Robot 2020;5(46):eabb9764.
[20] Won DO, Kim BD, Kim HJ, Eom TS, Müller KR, Lee SW. Curly: an AI-based curling robot successfully competing in the Olympic discipline of curling. In: Proceedings of the Twenty-Seventh International Joint Conference on Artificial Intelligence (IJCAI-18); 2018, 5883–5885.
[21] Znegui W, Gritli H, Belghith S. A new Poincaré map for investigating the complex walking behavior of the compass-gait biped robot. Appl Math Model 2021;94:534–57.
[22] Khan AT, Li S, Zhou X. Trajectory optimization of 5-link biped robot using beetle antennae search. IEEE Trans Circuits Syst II 2021;68(10):3276–80.
[23] Meng F, Huang Q, Yu Z, Chen X, Fan X, Zhang W, et al. Explosive electric actuator and control for legged robots. Engineering 2022;12:39–47.
[24] Jin B, Ye S, Su J, Luo J. Unknown payload adaptive control for quadruped locomotion with proprioceptive linear legs. IEEE/ASME Trans Mechatron 2022;27(4):1891–9.
[25] Song X, Zhang X, Meng X, Chen C, Huang D. Gait optimization of step climbing for a hexapod robot. J Field Robot 2022;39(1):55–68.
[26] Li H, Qi C, Gao F, Chen X, Zhao Y, Chen Z. Mechanism design and workspace analysis of a hexapod robot. Mech Mach Theory 2022;174:104917.
[27] Grzelczyk D, Awrejcewicz J. Dynamics, stability analysis and control of a mammal-like octopod robot driven by different central pattern generators. J Comput Appl Mech 2019;50(1):76–89.
[28] Cui L, Wang S, Zhang J, Zhang D, Lai J, Zheng Y, et al. Learning-based balance control of wheel-legged robots. IEEE Robot Autom Lett 2021;6(4):7667–74.
[29] Li J, Wu Q, Wang J, Li J. Neural networks-based sliding mode tracking control for the four wheel-legged robot under uncertain interaction. Int J Robust Nonlinear Control 2021;31(9):4306–23.
[30] Ni L, Wu L, Zhang H. Parameters uncertainty analysis of posture control of a four-wheel-legged robot with series slow active suspension system. Mech Mach Theory 2022;175:104966.
[31] Chen Z, Li J, Wang J, Wang S, Zhao J, Li J. Towards hybrid gait obstacle avoidance for a six wheel-legged robot with payload transportation. J Intell Robot Syst 2021;102(3):60.
[32] Chen Z, Li J, Wang S, Wang J, Ma L. Flexible gait transition for six wheel-legged robot with unstructured terrains. Robot Auton Syst 2022;150:103989.
[33] Gao F, Li S, Gao Y, Qi C, Tian Q, Yang GZ. Robots at the Beijing 2022 Winter Olympics. Sci Robot 2022;7(65):eabq0785.
[34] Zheng Y, Xu K, Tian Y, Ding X. Different manipulation mode analysis of a radial symmetrical hexapod robot with leg—arm integration. Front Mech Eng 2022;17(1):8.
[35] Wang G, Ding L, Gao H, Deng Z, Liu Z, Yu H. Minimizing the energy consumption for a hexapod robot based on optimal force distribution. IEEE Access 2020;8:5393–406.
[36] Ouyang W, Chi H, Pang J, Liang W, Ren Q. Adaptive locomotion control of a hexapod robot via bio-inspired learning. Front Neurorobot 2021;15:627157.
[37] Zhao Y, Gao F, Sun Q, Yin Y. Terrain classification and adaptive locomotion for a hexapod robot Qingzhui. Front Mech Eng 2021;16(2):271–84.
[38] Mao L, Gao F, Tian Y, Zhao Y. Novel method for preventing shin-collisions in six-legged robots by utilising a robot–terrain interference model. Mech Mach Theory 2020;151:103897.
[39] Arm P, Zenkl R, Barton P, Beglinger L, Dietsche A, Ferrazzini L, et al. SpaceBok: a dynamic legged robot for space exploration. In: Proceedings of 2019 International Conference on Robotics and Automation (ICRA); 2019 May 20–24; Montreal, QC, Canada. Piscataway: IEEE; 2019. p. 6288–94.
[40] Kolvenbach H, Hampp E, Barton P, Zenkl R, Hutter M. Towards jumping locomotion for quadruped robots on the moon. In: Proceedings of 2019 IEEE/RSJ International Conference on Intelligent Robots and Systems (IROS); 2019 Nov 03–08; Macau, China. Piscataway: IEEE; 2020. p. 5459–66.
[41] Boaventura T, Medrano-Cerda GA, Semini C, Buchli J, Caldwell DG. Stability and performance of the compliance controller of the quadruped robot HyQ. In: Proceedings of 2013 IEEE/RSJ International Conference on Intelligent Robots and Systems; 2013 Nov 03–07; Tokyo, Japan. Tokyo: IEEE; 2013. p. 1458–64.
[42] Yin K, Qi C, Gao Y, Sun Q, Gao F. Landing control method of a lightweight four-legged landing and walking robot. Front Mech Eng 2022;17(4):51.
[43] Penner AR. A scratch-guide model for the motion of a curling rock. Tribol Lett 2019;67(2):35.